



저작자표시-비영리-변경금지 2.0 대한민국

이용자는 아래의 조건을 따르는 경우에 한하여 자유롭게

- 이 저작물을 복제, 배포, 전송, 전시, 공연 및 방송할 수 있습니다.

다음과 같은 조건을 따라야 합니다:



저작자표시. 귀하는 원저작자를 표시하여야 합니다.



비영리. 귀하는 이 저작물을 영리 목적으로 이용할 수 없습니다.



변경금지. 귀하는 이 저작물을 개작, 변형 또는 가공할 수 없습니다.

- 귀하는, 이 저작물의 재이용이나 배포의 경우, 이 저작물에 적용된 이용허락조건을 명확하게 나타내어야 합니다.
- 저작권자로부터 별도의 허가를 받으면 이러한 조건들은 적용되지 않습니다.

저작권법에 따른 이용자의 권리는 위의 내용에 의하여 영향을 받지 않습니다.

이것은 [이용허락규약\(Legal Code\)](#)을 이해하기 쉽게 요약한 것입니다.

[Disclaimer](#)

이학박사학위논문

**Photonic crystal bandedge lasers:  
Biosensing application and new optical gain materials**

광자결정 띠가장자리 레이저:  
바이오센서 응용 및 새로운 광 이득 물질

2017년 2월

서울대학교 대학원  
생물물리 및 화학생물학과  
차형래



**Photonic crystal bandedge lasers:  
Biosensing application and new optical gain materials**

by  
Hyungrae Cha

*Supervised by*  
Professor Heonsu Jeon

*A Dissertation Submitted to the Faculty of  
Seoul National University  
in Partial Fulfillment of the Requirements  
for the Degree of  
Doctor of Philosophy*

February 2017

Department of Biophysics and Chemical Biology  
Graduate School  
Seoul National University



# Abstract

## **Photonic crystal bandedge lasers: Biosensing application and new optical gain materials**

Hyungrae Cha

Majoring in Biophysics

Department of Biophysics and Chemical Biology

The Graduate School

Seoul National University

Photonic crystals (PhCs) are periodic arrangements of two or more dielectric media. The periodicity of PhCs results in a complex photonic band structure which has a specific frequency region where a light does not propagate in a crystal. This is called a photonic band gap (PBG). By using PBG, a light can be strongly confined and following applications are available such as PhC cavity laser, filter, and waveguide. On the other hand, near the band edge in the band structure, the group velocity of the photon is close to zero. So, a standing wave is formed, and the interaction between the medium and the photon is very strong. By using this gain enhancement effect, a photonic crystal bandedge laser (BEL) can be implemented.

During my research years, I have been focused on different types of photonics crystal bandedge lasers because of following advantages such as stable mode operation over a large area, high power laser available, and controlling the lasing direction either surface-emitting or in-plane direction

which depends on its purpose of devices. With these advantages of PhC bandedge mode, I suggested various types of PhC bandedge lasers with different gain materials, and one of them for biosensing application.

In this thesis, air-bridge-type surface-emitting bandedge laser (BEL) was fabricated by forming a honeycomb lattice two-dimensional PhC structure into an InGaAsP multiple-quantum-well epilayer. Subsequently, the entire surface of bandedge laser was passivated with few-nm thick conformal SiO<sub>2</sub> layer by atomic layer deposition (ALD) method. In addition, the ALD-SiO<sub>2</sub> is compatible with the silane-based surface chemistry, enabling the ALD-passivated BEL devices as a label-free biosensor. From the standard streptavidin–biotin interaction sensing experiment, the device shows the possibility as refractive index biosensor platform with a sharp lasing line (< 0.2 nm) and large refractive index sensitivity (~163 nm/RIU).

Next, room temperature single mode bandedge laser was fabricated by hybridizing two-dimensional square lattice photonic crystal backbone with a perovskite thin film of methylammonium lead iodide (CH<sub>3</sub>NH<sub>3</sub>PbI<sub>3</sub>) spin-coated atop. Also, from the hybridizing the hybrid perovskite CH(NH<sub>2</sub>)<sub>2</sub>Pb(Br<sub>0.6</sub>I<sub>0.4</sub>)<sub>3</sub> thin film with one-dimensional photonic crystal structure backbone by simple spin-casting, single mode bandedge laser was demonstrated. I believe that these hybrid photonic device platforms with optical pumping show the possibility of electrically driven laser device with perovskite materials in the near future.

**Keyword:** Photonic crystal, Photonic crystal bandedge laser, Biosensing application, Hybrid perovskite thin film, Hybrid photonics, Spin-casting

**Student number:** 2010-24018

# Contents

## Chapter 1

<b>Introduction</b>	1
1.1 Photonic crystals	1
1.1.1 Introduction	1
1.1.2 Photonic band structure	3
1.1.3 Photonic crystal bandedge laser	5
1.2 Perovskite material as new optical gain medium	7
1.2.1 Organic-inorganic lead halide perovskite	7
1.3 Computational method	10
1.3.1 Plane wave expansion method	10
1.3.2 Finite difference time domain method	11
1.4 Outline of the manuscript	12
References	14

## Chapter 2

### Surface passivation of photonic crystal bandedge laser by atomic

<b>layer deposition of SiO<sub>2</sub> and its application for biosensing</b>	----- 17
2.1 Introduction	----- 17
2.2 Photonic crystal bandedge laser	----- 19
2.2.1 2D honeycomb lattice photonic crystal bandedge laser	----- 19
2.2.2 Device fabrication	----- 22
2.3 ALD surface passivation	----- 24
2.3.1 Atomic layer deposition	----- 24
2.3.2 ALD-SiO <sub>2</sub> passivation procedure	----- 26
2.3.3 ALD-SiO <sub>2</sub> passivation layer on the performance of PhC BEL	---- 27
2.4 Biosensing results and discussion	----- 32
2.4.1 Biosensing preparation with streptavidin-biotin interaction	----- 32
2.4.2 Measurement	----- 36
2.5 Summary	----- 39
References	----- 40

## Chapter 3

### Two-dimensional photonic crystal bandedge laser with hybrid

<b>perovskite thin film for optical gain</b> .....	45
3.1 Introduction .....	45
3.2 2D square lattice photonic crystal bandedge laser .....	47
3.2.1 Photonic crystal bandedge mode .....	47
3.2.2 Device fabrication .....	48
3.2.3 Photonic band structure of perovskite PhC bandedge laser .....	52
3.3. Results and discussion .....	54
3.3.1 Measurement with polarization dependence .....	54
3.4 Summary .....	57
References .....	58

## Chapter 4

### Visible wavelength distributed feedback laser from formamidinium lead

<b>halide perovskite thin films with TE/TM mode selection</b> -----	61
4.1 Introduction -----	61
4.2 1D DFB laser with perovskite $\text{FAPb}(\text{Br}_{0.6}\text{I}_{0.4})_3$ -----	63
4.2.1 Preparation of $\text{CH}(\text{NH}_2)_2\text{Pb}(\text{Br}_{0.6}\text{I}_{0.4})_3$ perovskite material -----	63
4.2.2 Device fabrication -----	66
4.2.3 TE/TM mode selection -----	70
4.3. Results and discussion -----	73
4.3.1 Measurement with polarization dependence -----	73
4.3.2 Temperature dependence for $\text{FAPb}(\text{Br}_{0.6}\text{I}_{0.4})_3$	
1D DFB laser and PL -----	76
4.4 Summary -----	78
4.5 Supporting information -----	79
References -----	80

## Chapter 5

<b>Conclusion and perspective</b> -----	85
---	----

Abstract in Korean -----	87
--------------------------	----

# List of Figures

Figure 1-1-1 Simple examples of 1D, 2D, and 3D PhCs and their SEM images with sub-micron periods. -----	2
Figure 1-1-2 Photonic band structure of a 2D hexagonal lattice PhC.-----	3
Figure 1-1-3 Free-standing GaN-based photonic crystal bandedge laser.-----	5
Figure 1-1-4 Two-dimensional hexagonal lattice photonic crystal bandedge laser patterned by nanosphere lithography. -----	6
Figure 1-2-1 The schematic crystal structure of lead halide perovskites $APbX_3$ , A = FA or MA, X = I, Br, or Cl. -----	7
Figure 1-2-2 Wide wavelength tunability of ASE wavelengths from organic–inorganic halide perovskite films. -----	8
Figure 1-2-3 Four general methods for preparing perovskite active layers. ----	9
Fig. 2-2-1 (a) Photonic band structure of a 2D honeycomb lattice PhC. Magnetic field (Hz) profile calculated at the two different $\Gamma$ points: (b) dipole-like $\Gamma_2$ mode and (c) monopole-like $\Gamma_1$ mode. SEM images of a 2D honeycomb lattice PhC patterns: (d) top view and (e) tilted view at a higher magnification. -----	20
Fig. 2-2-2 Schematic diagram of InGaAsP MQW structure. -----	23
Fig. 2-2-3 Fabrication processes of PhC bandedge laser. -----	23
Fig. 2-3-1 Cross-sectional TEM image of an ALD-SiO <sub>2</sub> layer deposited on an InP bare substrate. -----	28
Fig. 2-3-2 SEM image of an InP circular mesa etched in a diluted HCl solution with the mesa top protected by the ALD-SiO <sub>2</sub> layer. Inset is another SEM	

image of the circular mesa taken from the top. -----	28
Figure 2-3-3 Schematic diagram of fiber based micro-PL setup. -----	30
Figure 2-3-4 Lasing spectra from an InGaAsP MQW BEL device, taken at different stages of sample treatments. -----	31
Figure 2-3-5 Input power vs. output power relations of a typical BEL device. -----	31
Figure 2-4-1 Schematic diagram of surface functionalization steps for biosensing test. From the top, 2D PhC BEL fabrication; conformal deposition of an ALD-SiO <sub>2</sub> layer; biotinylation on the silica-terminated surface; and the interaction between biotin and streptavidin molecules tagged with fluorescence dye (SAPE). -----	34
Figure 2-4-2 Fluorescence microscopy image taken after the streptavidin-biotin interaction. -----	35
Figure 2-4-3 Lasing spectra of positively controlled BEL biosensors before and after the streptavidin-biotin interaction: (a) dipole-like mode and (b) monopole-like mode. -----	36
Figure 2-4-4 Lasing spectra of negatively controlled (biotin-free) BEL biosensors before and after the streptavidin treatment: (a) dipole-like mode and (b) monopole-like mode. -----	37
Figure 3-1-1 Halide perovskite materials for photonic applications with various cavity geometries. -----	46
Figure 3-2-1 (a) Schematic of the CH <sub>3</sub> NH <sub>3</sub> PbI <sub>3</sub> PhC bandedge laser structure. (b) SEM image of the square lattice PhC backbone, fabricated on the Si <sub>3</sub> N <sub>4</sub> layer with (b) low and (c) high magnifications. The SEM images are from	

gamma point bandedge laser sample:  $a_{\Gamma} = 345$  nm and  $\phi_{\Gamma} = 150$  nm. A reciprocal lattice of square lattice is schematically drawn in (b). ----- 49

Figure 3-2-2 Fabrication processes of PhC bandedge laser with perovskite thin film. ----- 50

Figure 3-2-3 Optical microscope images taken (a) before and (b) after the deposition of  $\text{CH}_3\text{NH}_3\text{PbI}_3$  thin film. In (a), the bright square region in the middle corresponds to the PhC patterned area. SEM images of a fully fabricated  $\text{CH}_3\text{NH}_3\text{PbI}_3$  PhC bandedge laser device: (c) top surface of the perovskite film and (d) cross-section of the device, shown sequentially from  $\text{SiO}_2$  to  $\text{CH}_3\text{NH}_3\text{PbI}_3$  thin film. The dotted lines in (b) and (d) are for eye-guide. ----- 51

Figure 3-2-4 (a) Photonic band structure of the  $\text{CH}_3\text{NH}_3\text{PbI}_3$  PhC bandedge laser structure, calculated by the plane-wave expansion method. Also shown in the right are magnified band structures near (b)  $\Gamma$ - and (c) M-points, which are marked by square boxes in (a). ----- 53

Figure 3-2-5 Mode spectra for (a) sample  $\Gamma$  and (b) sample M, both simulated by FDTD method. For each case, the inset shows the modal pattern calculated for the strongest bandedge mode. ----- 53

Figure 3-3-1 Schematic diagram of lens based micro-PL setup. ----- 54

Figure 3-3-2 Emission spectra from the  $\text{CH}_3\text{NH}_3\text{PbI}_3$  PhC bandedge lasers recorded at various excitation levels: (a) sample  $\Gamma$  and (b) sample M. Each inset presents the relationship between light input and output. Measured polarization dependence of light output: (c) sample  $\Gamma$  and (d) sample M. The directions of the reciprocal lattice vectors ( $\Gamma$ , X, and M) are marked. --- 56

Figure 4-2-1 Photoluminescence of different FA-based perovskite thin film from 550 nm to 900 nm. -----	64
Figure 4-2-2 Scanning electron microscopy (SEM) and atomic force microscopy (AFM) of $\text{FAPb}(\text{Br}_{0.6}\text{I}_{0.4})_3$ film. -----	65
Figure 4-2-3 Crystal information of $\text{FAPb}(\text{Br}_{0.6}\text{I}_{0.4})_3$ perovskite thin film from X-ray diffractometer (XRD). -----	65
Figure 4-2-4 (a) Schematic of the $\text{CH}(\text{NH}_2)_2\text{Pb}(\text{Br}_{0.6}\text{I}_{0.4})_3$ 1D DFB laser structure. (b) Scanning electron microscopy (SEM) images from the fabricated 1D grating pattern on quartz substrate. -----	68
Figure 4-2-5 (a) Cross sectional SEM image of local area of the sample after hybrid perovskite $\text{CH}(\text{NH}_2)_2\text{Pb}(\text{Br}_{0.6}\text{I}_{0.4})_3$ thin film (b) demonstrating optical transparency of the thin film (c) photographic image of 1D grating pattern. -----	68
Figure 4-2-6 Schematic of the LIL setup based on a Lloyd's mirror interferometer and fabricated 1D grating on quartz substrate. -----	69
Figure 4-2-7 Mode spectra for (a) TE mode and (b) TM mode, by FDTD simulation. -----	71
Figure 4-2-8 Mode profiles for (a) TE mode and (b) TM mode. These are well-defined TE/TM fundamental modes by the structure. -----	72
Figure 4-3-1 Schematic diagram of cylindrical lens based PL setup. -----	73
Figure 4-3-2 Emission spectra from the $\text{CH}(\text{NH}_2)_2\text{Pb}(\text{Br}_{0.6}\text{I}_{0.4})_3$ 1D DFB laser at various excitation levels: (a) TE and (b) TM mode. Each inset shows the relationship between light input and output. Measured polarization dependence of light output: (c) TE and (b) TM mode. -----	75

Figure 4-3-3 Temperature-dependent relationship between light input and output of  $\text{CH}(\text{NH}_2)_2\text{Pb}(\text{Br}_{0.6}\text{I}_{0.4})_3$  1D DFB laser for TM mode. ----- 77

Figure 4-3-4 Temperature-dependent PL spectra of  $\text{CH}(\text{NH}_2)_2\text{Pb}(\text{Br}_{0.6}\text{I}_{0.4})_3$  thin film. ----- 77

Figure 4-5-1 Single mode lasing operation with the one-dimensional photonic crystal structure at different wavelength regime. ----- 79



# Chapter 1

## Introduction

### 1.1 Photonic crystals

#### 1.1.1 Introduction

Photonic crystals (PhCs) are periodic arrangements of two or more dielectric media [1]. According to the periodicity of media, PhCs are defined as one-, two-, and three-dimensional PhC structures. Figure 1-1-1 shows different types of PhC structures with scanning electron microscope (SEM) images, respectively [2].

In general, within a homogeneous material, the dispersion relation between wave vector  $\mathbf{k}$  and frequency  $\omega$  is expressed as

$$\omega(k) = \frac{ck}{\sqrt{\epsilon}}$$

where  $\epsilon$  is a dielectric constant. However, in a periodically arranged structure like a photonic crystal, the dispersion relation changes nonlinearly, and in a certain condition, the discontinuous frequency region which is called the photonic bandgap appears. It can be understood as a mechanism similar to form electronic band where electrons cannot have a specific energy by the periodic potential of the atoms making up solid crystals.

The way that light propagates in photonic crystals is described by the wave equation obtained from the Maxwell equation as follows.

$$\nabla \times [\epsilon(\vec{r})^{-1} \nabla \times \vec{H}(\vec{r})] - \frac{\omega^2}{c^2} \vec{H}(\vec{r}) = 0 \quad \vec{H}(\vec{r}, t) = \vec{H}(\vec{r}) e^{-i\omega t}$$

When the dielectric constant epsilon is given by a periodic function with a position, magnetic field (H field) can be described as a bloch form by plane wave expansion and bloch theorem.

$$\epsilon(\vec{r}) = \epsilon(\vec{r} + \vec{R}) \quad (\vec{R} : \text{Lattice vector}) \quad \vec{H}_{\vec{k}}(\vec{r}) = \sum_{\vec{G}} c_{\vec{G}} e^{i(\vec{k} + \vec{G}) \cdot \vec{r}}$$

$$\omega = \omega(\vec{k}) \quad (\text{dispersion relation})$$

When solving the eigenvalue problem, the dispersion relation like above can be obtained, and the information contained in these functions is called the photonic crystal band structure with photonic bandgap.

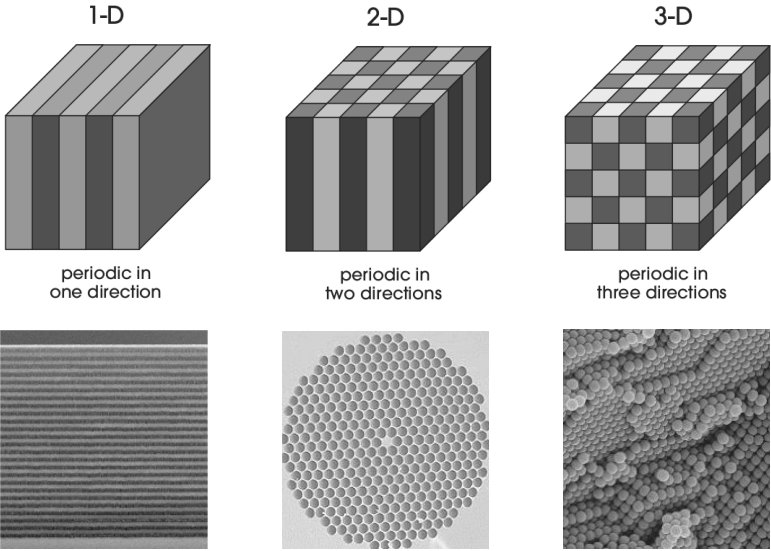


Fig. 1-1-1 Simple examples of 1D, 2D, and 3D PhCs [1] and their SEM images with sub-micron periods [2].

### 1.1.2 Photonic band structure

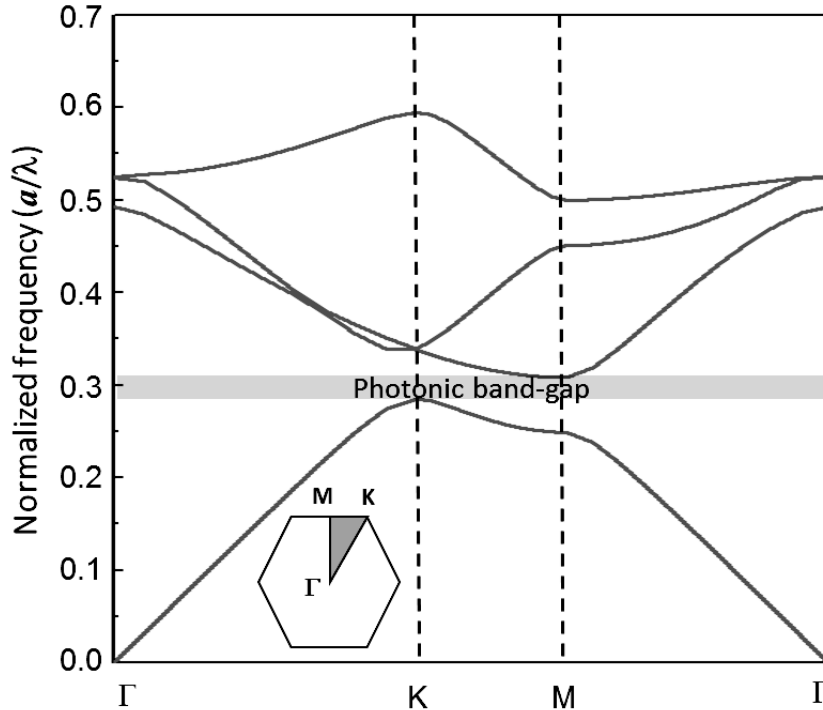


Fig. 1-1-2 Photonic band structure of a 2D hexagonal lattice PhC.

The concept of photonic crystal bandedge lasers (BELs) is first reported by Dowling [3]. Figure 1-1-2 is the photonic band structure with two-dimensional hexagonal lattice. In the band structure, there is a frequency region where no mode can exist in the crystal. This region is called photonic band gap (PBG). By using PBG, a light can be strongly confined and following applications are available such as photonic crystal cavity laser [3,4], filter [5], and waveguide [6,7]. In the case of a cavity laser, photon whose frequency is in the photonic band gap is confined horizontally by the band gap and vertically by the index guiding in a defect. If the defect has a gain medium, the structure supports a lasing action. This is how a photonic crystal cavity laser is designed.

On the other hand, near the band edge, photon's group velocity is close to zero. So, optical path length is exceedingly long in the structure, which lead to a gain enhancement. This gain enhancement effect uses for making photonic band edge laser and such a structure does not need to contain any defect. In this thesis, I suggested various types of PhC bandedge lasers with different gain materials, and one of them for biosensing application.

### 1.1.3 Photonic crystal bandedge laser

The photon crystal band edge laser generated by previous bandedge principle has the following advantages: First, it is possible to realize a stable mode operation over a large area without requiring a large difference in refractive indices. Second, as the bandedge mode spreads widely over a larger area, high output power laser is possible because the amount of local heat generation is small. Finally, by controlling the lasing direction either surface-emitting or in-plane direction, the design and use of the device is little more flexible depending on their purpose. There are some examples of different types of bandedge lasers in Fig. 1-1-3 [8] and 1-1-4 [9].

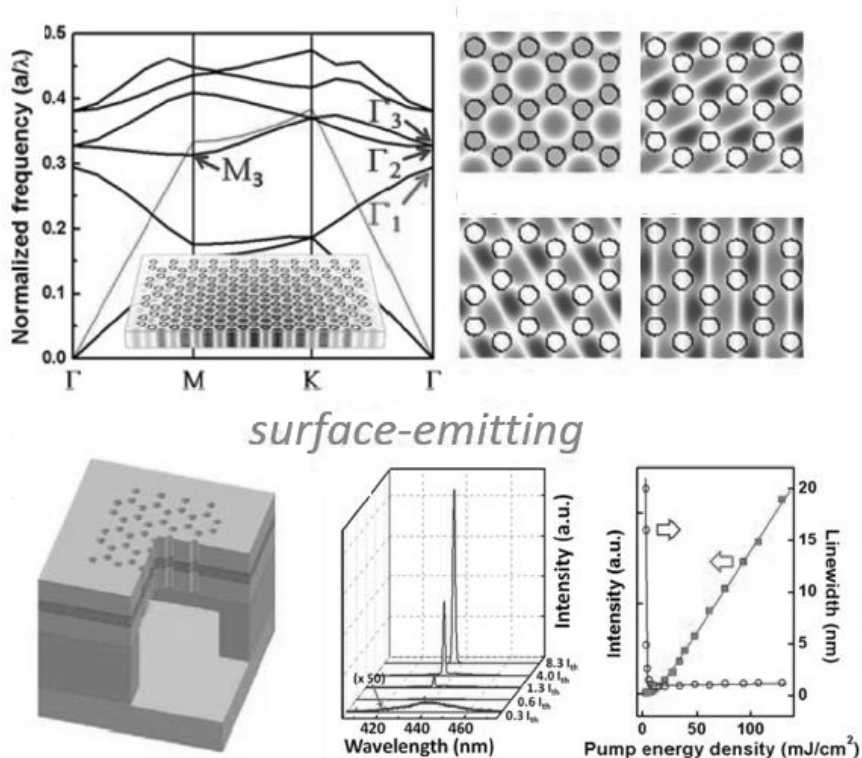


Fig. 1-1-3 Free-standing GaN-based photonic crystal bandedge laser [8].

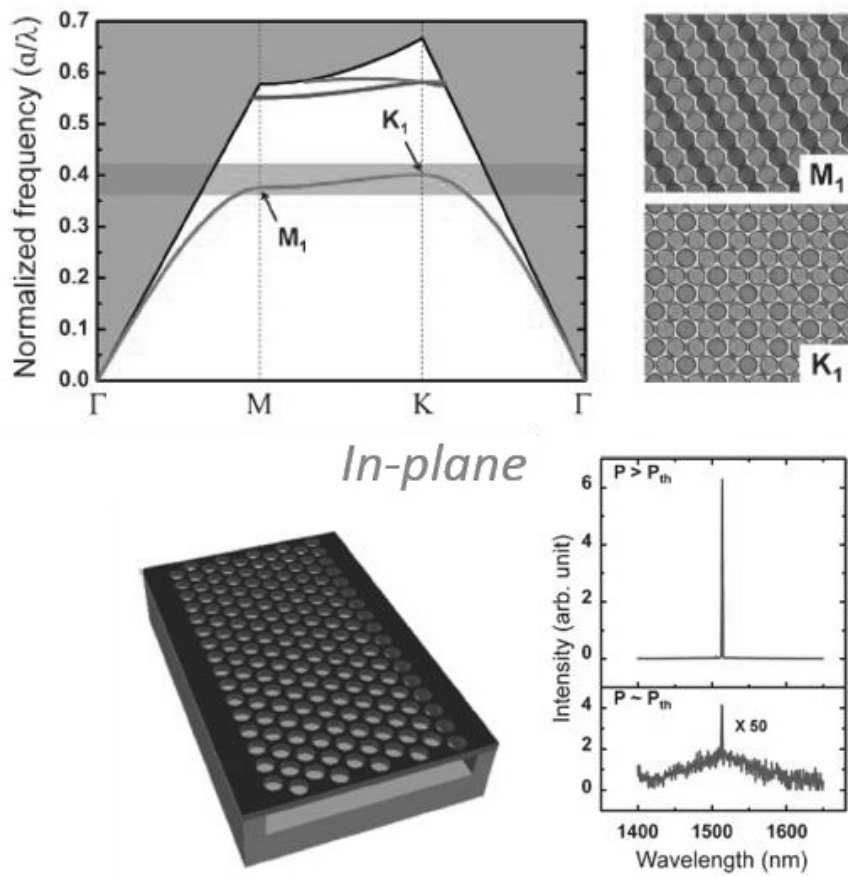


Fig. 1-1-4 Two-dimensional hexagonal lattice photonic crystal bandedge laser patterned by nanosphere lithography [9].

## 1.2 Perovskite material as new optical gain medium

### 1.2.1 Organic-inorganic lead halide perovskite

In photovoltaics, hybrid perovskite (*e.g.*  $\text{CH}_3\text{NH}_3\text{PbI}_3$ ) is promising light-absorbing materials and its superior properties such as strong light harvesting capability, direct band gap, high carrier mobility, etc. [10] fascinate many researching groups. Notably, Kojima group employed the hybrid perovskites as a light absorber of photovoltaic cells (PVCs), achieving the power conversion efficiency (PCE) of  $\sim 4\%$  [11]. The PCE of the hybrid perovskite PVCs is now more than 20% [12]. Due to the predominant properties, hybrid perovskite is widely studied in optical, electronic, photovoltaic research area. The hybrid lead perovskite structure has the general stoichiometry of  $\text{APbX}_3$ , where “A” are cations and “X” are anions in Fig. 1-2-1 [13].

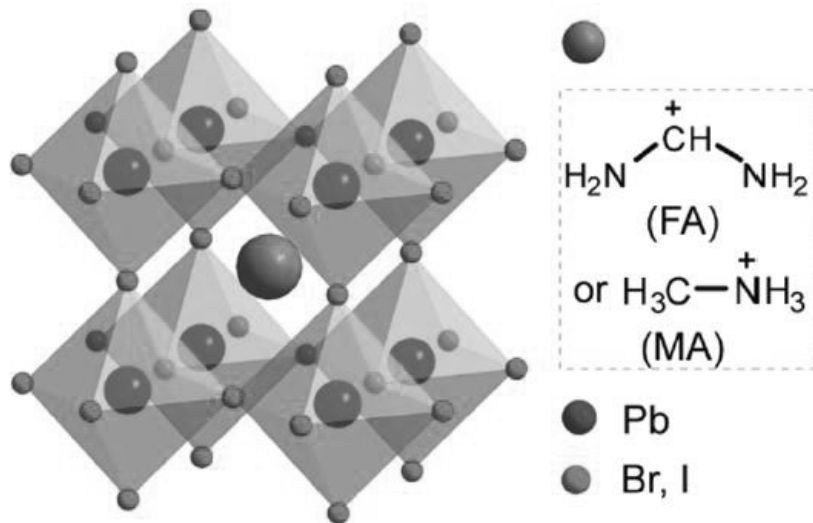


Fig. 1-2-1 The schematic crystal structure of lead halide perovskites  $\text{APbX}_3$ , A = FA or MA, X = I, Br, or Cl [13].

The reason why this perovskite gets attention in the field of solar cell with long carrier lifetime and diffusion length [14], the high internal quantum efficiency [15], and large absorption coefficient across the uv-visible range [16]. As previous mentioned, perovskite materials have been used as light absorbers, which in turn infer that they could also act as efficient light emitters in optoelectronic device. In particular, the properties of high photoluminescence (PL) quantum efficiency and stoichiometric wavelength tunability show a simple indication of how attractive this material is as a light emitter. Figure 1-2-2 shows the wavelength tunability with different halide compositions of organic-inorganic halide perovskite film from 400 nm to 800 nm [17].

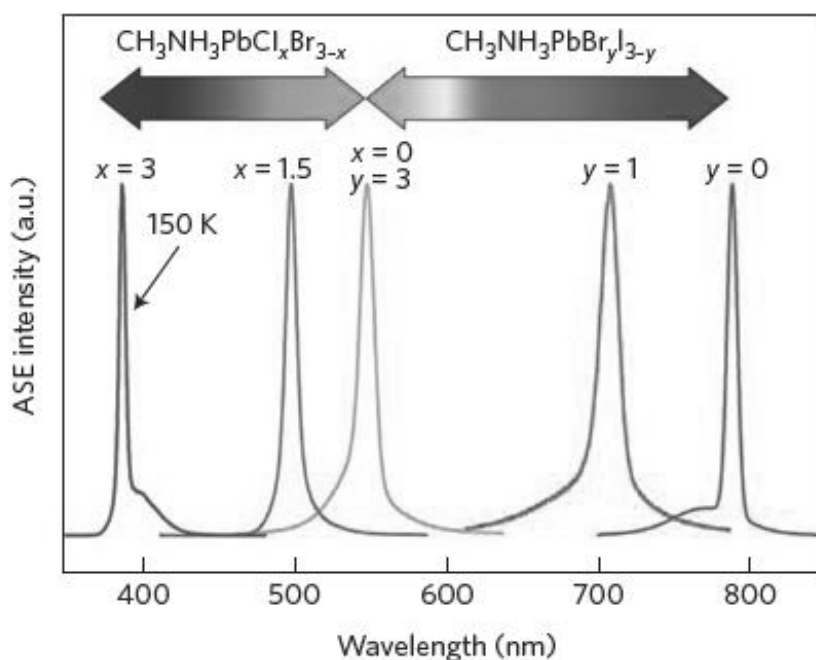


Fig. 1-2-2 Wide wavelength tunability of ASE wavelengths from organic–inorganic halide perovskite films [17].

There are four general deposition techniques for preparing perovskite active layers in Fig. 1-2-3 [18]. Two methods are based on solution process, and the others are based on evaporation process. In this thesis, passive photonic crystal structures were hybridized extrinsically with hybrid lead perovskite thin film by one-step deposition method like simple spin-casting. This simple spin-casting method has some advantages such as large area, cost effective, and high throughput. Due to the uncontrolled solidification, a low film coverage is a well-known problem of one-step deposition method, but we solved this problem through solvent engineering method [19].

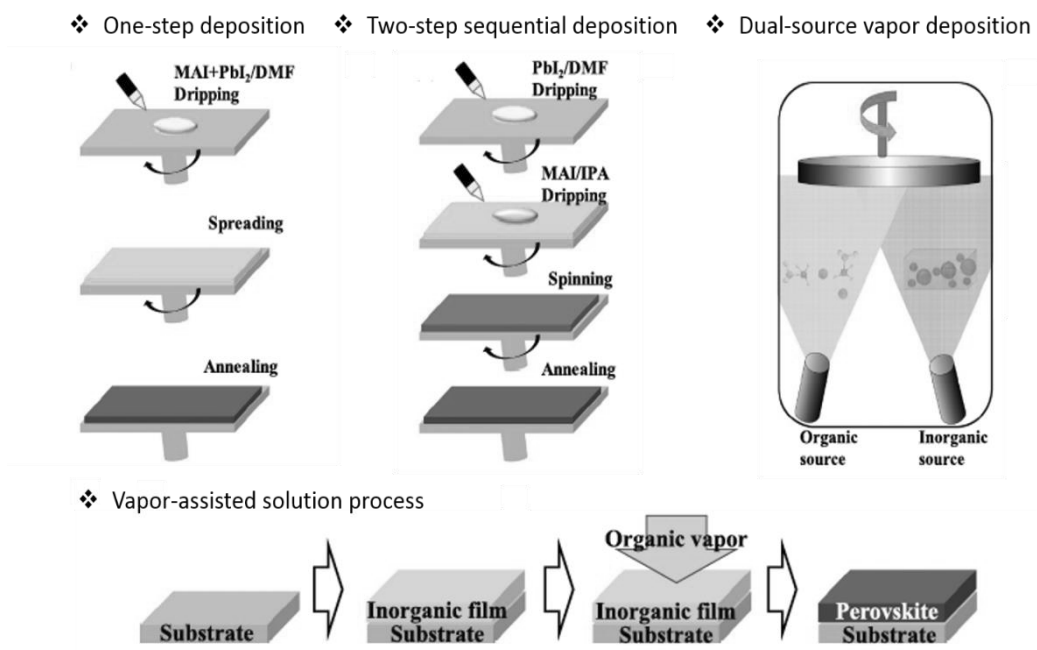


Fig. 1-2-3 Four general methods for preparing perovskite active layers [18].

## 1.3 Computational Method

### 1.3.1 Plane wave expansion method

In the photonic crystal community, the Plane Wave Expansion (PWE) method refers to a very powerful technique, and it is suitable for investigating the photonic band structure (dispersion relation) of all kinds of PhCs and the modal solution problem. Also, this computation is quick and easy to manipulate. To solve the Maxwell equations, the electric or magnetic fields are expanded for each field component in the side of the Fourier series components along the reciprocal lattice vector. These differential equations result in an infinite size matrix eigenvalue problem, which can be solved by an appropriate approximation [20,21].

In this thesis, two-dimensional photonic crystal band structures were obtained by using commercially available computer software, BandSOLVE (Rsoft Design Group), which is based on the PWE simulation method.

### 1.3.2 Finite difference time domain

The finite difference time domain method (FDTD) is one of the most effective technique for the solution of electromagnetic problems in the study of photonics recently. This numerical analysis is extremely simple, even for programming three-dimensional code. To solve an electromagnetic problem, the idea is to simply discretize in space which is divided into discrete grid like mesh, and in time step which the electric and magnetic field are developed. Unlike the previous PWE method, we can put a source signal, and investigate time dynamics of the motion of the photons which are generated from dipole source in a structure. The solution-dependent Maxwell equations with central difference approximations can be solved accurately depending on the size of the lattice and time step [22].

Due to advantages of the FDTD method, there are many kinds of computer software products has been developed commercially, and in this thesis, Lumerical FDTD Solutions (Lumerical Solutions, Inc.) was used to explore the photonic band structures, wavelength spectrums, and electric field profiles of each PBE modes.

## 1.4 Outline of the Manuscript

In this thesis, I proposed various types of PhC bandedge lasers with different gain materials and one of them for biosensing application. With following gain materials, InGaAsP MQW ( $\lambda \sim 1550$  nm), methylammonium (MA) lead triiodide perovskite material ( $\text{CH}_3\text{NH}_3\text{PbI}_3$ ,  $\lambda \sim 780$  nm), and formamidinium (FA) based  $\text{CH}(\text{NH}_2)_2\text{Pb}(\text{I}_{0.4}\text{Br}_{0.6})_3$  perovskite material ( $\lambda \sim 650$  nm), different types of PhC bandedge lasers were designed to operate in single mode, and the resonance wavelength is covered from visible to near-infrared (NIR). PhC bandedge lasers were also fabricated for their own purpose, and through the micro-PL measurement, we could analyze the lasing properties including polarization dependences.

In chapter 2, air-bridge-type surface-emitting bandedge laser was suggested for applying as refractive index biosensor. The entire surface of bandedge laser was passivated with few-nm thick conformal  $\text{SiO}_2$  layer by atomic layer deposition (ALD) method. In addition, the ALD- $\text{SiO}_2$  is compatible with the silane-based surface chemistry, enabling the ALD-passivated BEL devices as a label-free biosensor. Through the simple streptavidin–biotin interaction sensing experiment, the device shows the possibility as refractive index biosensor platform.

In chapter 3 and 4, PhC bandedge lasers were demonstrated by hybridizing passive PhC structures with hybrid perovskite materials by simple spin-casting method. The single mode bandedge lasers were operated via photonic bandedge modes, and this was verified by comparing the polarization dependence measurement and PL spectrum data to FDTD simulation result. From the results of these hybrid photonic device platforms with optical pumping, they show the possibility of electrically driven laser device with perovskite materials in the near future.

Finally in chapter 5, the conclusion and the perspectives are presented, and the acknowledgement is also shown.

## References

- [1] John D. Joannopoulos, Robert D. Meade, and Joshua N. Winn, *Photonic crystals: Molding the flow of light* (Princeton University Press 2008).
- [2] <http://mnoel.snu.ac.kr/>
- [3] H. Yokoyama, "Physics and device applications of optical microcavities," *Science*, **256**, 66-70, (1992).
- [4] O. Painter, R. K. Lee, A. Scherer, A. Yariv, J. D. O'Brien, P. D. Dapkus, and I. Kim, "Two-dimensional photonic band-gap defect mode laser," *Science*, **284**, 1819-1821, (1999).
- [5] O. Akahane, T. Asano, H. Takano, B.-S. Song, Y. Takana, and S. Noda, "Two-dimensional photonic-crystal-slab channel-drop filter with flat-top response," *Optics Express*, **13**, 2512-2530, (2005).
- [6] C. J. M. Smith, H. Benisty, S. Olivier, M. Rattier, C. Weisbuch, T. F. Krauss, R. M. De La Rue, R. Houdré, and U. Oesterle, "Low-loss channel waveguides with two-dimensional photonic crystal boundaries," *Applied Physics Letters*, **77**, 2813-2815, (2000).
- [7] Y.-G. Roh, S. Yoon, H. Jeon, S.-H. Han, and Q.-H. Park, "Experimental verification of cross talk reduction in photonic crystal waveguide crossings," *Applied Physics Letters*, **85**, 3351-3353, (2004).
- [8] D.-U. Kim, S. Kim, J. Lee, S.-R. Jeon, and H. Jeon, "Free-standing GaN-based photonic crystal band-edge laser," *Photonics Technology Letters, IEEE*, **23**, 1454-1456, (2011).
- [9] S. Ahn, H. Kim, H. Jeon, J. R. Oh, Y. R. Do, and H. J. Kim, "Two-dimensional

- hexagonal lattice photonic crystal band-edge laser patterned by nanosphere lithography,” *Applied Physics Express*, **5**, 042102, (2012).
- [10] M. A Green, Y. Jiang, A. M. Soufiani, and A. Ho-Baillie, “Optical properties of photovoltaic organic–inorganic lead halide perovskites,” *The Journal of Physical Chemistry Letters*, **6**, 4774-4785, (2015).
- [11] A. Kojima, K. Teshima, Y. Shirai, and T. Miyasaka, “Organometal halide perovskites as visible-light sensitizers for photovoltaic cells,” *Journal of the American Chemical Society*, **131**, 6050-6051, (2009).
- [12] W. S. Yang, J. H. Noh, N. J. Jeon, Y. C. Kim, S. Ryu, J. Seo, and S. I. Seok, “High-performance photovoltaic perovskite layers fabricated through intramolecular exchange,” *Science*, **348**, 1234-1237, (2015).
- [13] Y. Fu, H. Zhu, A. Schrader, D. Liang, Q. Ding, P. Joshi, L. Hwang, X-Y Zhu, and S. Jin, “Nanowire lasers of formamidinium lead halide perovskites and their stabilized alloys with improved stability,” *Nano Letters*, **16**, 1000-1008, (2016).
- [14] S. D Stranks, G. E Eperon, G. Grancini, C. Menelaou, M. JP Alcocer, T. Leijtens, L. M Herz, A. Petrozza, and H. J Snaith, “Electron-hole diffusion lengths exceeding 1 micrometer in an organometal trihalide perovskite absorber,” *Science*, **342**, 341-344, (2013).
- [15] F. Deschler, M. Price, S. Pathak, L. E Klintberg, D.-D. Jarausch, R. Higler, S. Hüttner, T. Leijtens, S. D Stranks, and H. J Snaith, “High photoluminescence efficiency and optically pumped lasing in solution-processed mixed halide perovskite semiconductors,” *The Journal of Physical Chemistry Letters*, **5**, 1421-1426, (2014).
- [16] J. Chen, S. Zhou, S. Jin, H. Li, and T. Zhai, “Crystal organometal halide

- perovskites with promising optoelectronic applications,” *Journal of Materials Chemistry C*, **4**, 11-27, (2016).
- [17] G. Xing, N. Mathews, S. S. Lim, N. Yantara, X. Liu, D. Sabba, M. Grätzel, S. Mhaisalkar, and T. C. Sum, “Low-temperature solution-processed wavelength-tunable perovskites for lasing,” *Nature Materials*, **13**, 476-480, (2014).
- [18] J. Cui, H. Yuan, J. Li, X. Xu, Y. Shen, H. Lin, and M. Wang, “Recent progress in efficient hybrid lead halide perovskite solar cells,” *Science and Technology of Advanced Materials*, **16**, 1-14, (2015).
- [19] N. J. Jeon, J. H. Noh, Y. C. Kim, W. S. Yang, S. Ryu, and S. I. Seok, “Solvent engineering for high-performance inorganic–organic hybrid perovskite solar cells,” *Nature materials*, **13**, 897-903, (2014).
- [20] K.-M. Ho, C. T. Chan, and C. M. Soukoulis, “Existence of a photonic gap in periodic dielectric structures,” *Physical Review Letters*, **65**, 3152, (1990).
- [21] R. D. Meade, A. M. Rappe, K. D. Brommer, J. D. Joannopoulos, and O. L. Alerhand, “Accurate theoretical analysis of photonic band-gap materials,” *Physical Review B*, **48**, 8434, (1993).
- [22] K. S. Yee, “Numerical solution of initial boundary value problems involving Maxwell’s equations in isotropic media,” *IEEE Transactions on Antennas Propagation*, **14**, 302, (1996).

## Chapter 2

# Surface passivation of a photonic crystal bandedge laser by atomic layer deposition of SiO<sub>2</sub> and its application for biosensing

### 2.1 Introduction

Biosensors have now become a popular application field, as various sensor platforms which are based on different technologies such as mechanics [1,2], electricity [3-5], optics [6], etc. In particular, optical (or photonic) biosensors have many advantages over other types of sensor devices; they are non-destructive and insensitive to electrical conductivity, salt concentration, or pH of assay solution. Optical biosensors are also compatible with optofluidics technology so that a complete sensing system with *in situ* detection and analysis capabilities can be built in a compact and versatile format. It has been proven that optical sensor devices, when combined with micro and nano-scale structures, such as microdisk [7], microring [8], grating [9], photonic crystal (PhC) [10-12], and nanoplasmonics [13,14], can provide an ultra-high sensitivity owing to enhanced interaction between photons and matters. In this study, we demonstrate a photonic crystal based nanolaser device and its surface passivation with an atomically thin layer, which leads to a highly sensitive, compact, and yet robust biosensor platform.

Rapid progress has been made in developing PhC-based nanolasers, both in their

structural designs and performance characteristics, which makes them quite promising for compact coherent light sources of the future [15,16]. In order for the PhC based nanolasers to become a viable device platform, however, a number of issues are still to be further matured, which include electrical injection [17], continuous-wave operation [18], and high power operation [19]. In addition, an appropriate passivation of device surface is practically an important issue to be addressed for long-term device longevity as well as for device protection from harsh environmental conditions that may be encountered in course of real applications of device. Here, we applied atomic layer deposition (ALD) to deposit a ultra-thin (in the scale of a few nanometers) and conformal SiO<sub>2</sub> layer onto a two-dimensional (2D) PhC nanolaser structure of complex surface topography. Resultant nanolasers are found to be resistant to the wet chemicals that would otherwise spontaneously demolish the nanolaser composed of compound semiconductors. The effectiveness and significance of the ALD passivation are vividly demonstrated by employing the ALD-passivated PhC nanolasers as a label-free protein detector. Significantly, the biosensor based on the nanolasers takes the advantage of the extremely sharp resonance peak of PhC nanolasers and shows a figure of merit (FOM) of ~800, which is more than 10 times larger than those of previous optical biosensors. This result clearly shows that our scheme is a viable method for building highly sensitive biosensors based on PhC nanolaser structures.

## 2.2 Photonic crystal bandedge laser

### 2.2.1 2D honeycomb lattice photonic crystal bandedge laser

In this experiment, we utilized bandedge lasers (BEL) as our standard PhC-based nanolaser structure, which was composed of an air-bridge membrane slab of an InGaAsP multiple quantum well (MQW) epilayer with a 2D honeycomb-lattice array of air-holes. A BEL, especially when operated at the  $\Gamma$ -point, has several advantages over a defect-containing cavity-based PhC laser structure; it has a large modal volume which is available for high output power and gives vertical laser emission, both properties facilitating detection of laser emission off from the wafer plane. In addition, a BEL has an infinite translational symmetry so that a delicate optical alignment procedure required for exciting a cavity-based PhC laser can be greatly simplified or omitted.

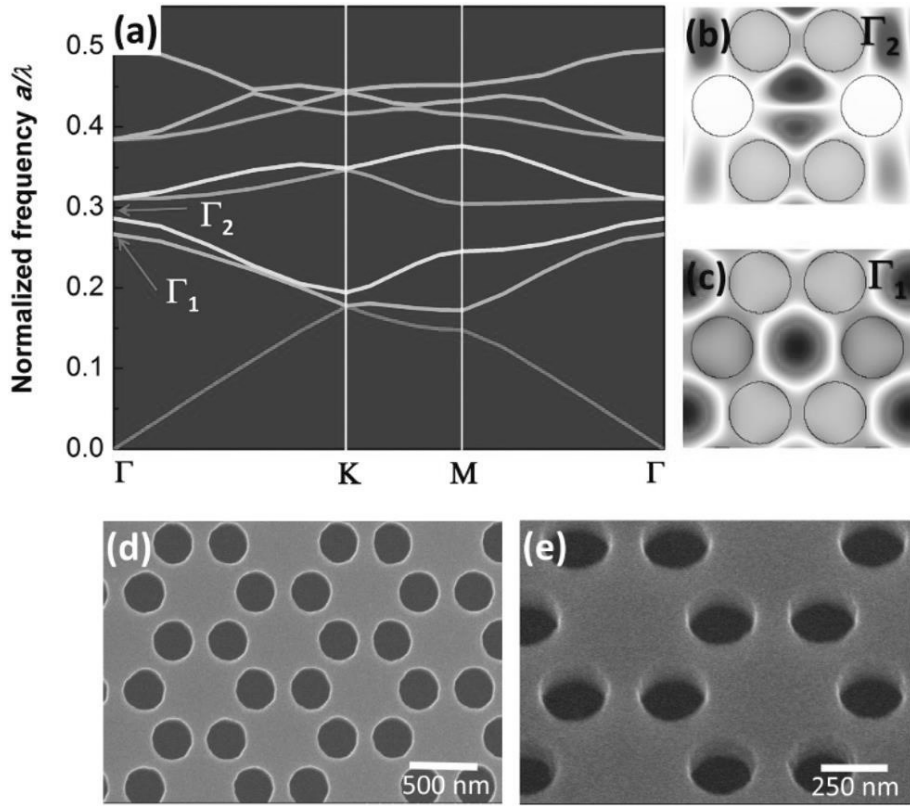


Fig. 2-2-1 (a) Photonic band structure of a 2D honeycomb lattice PhC. Magnetic field (Hz) profile calculated at the two different  $\Gamma$  points: (b) dipole-like  $\Gamma_2$  mode and (c) monopole-like  $\Gamma_1$  mode. SEM images of a 2D honeycomb lattice PhC patterns: (d) top view and (e) tilted view at a higher magnification.

As for the PhC pattern, we fixed the air-hole radius as  $r = 0.35a$ , where  $a$  is the lattice constant of honeycomb-lattice PhC. Figure 2-2-1(a) shows photonic band structure of the honeycomb-lattice 2D PhC, which is calculated by using the plane wave expansion (PWE) method. There are two  $\Gamma$ -point bandedge modes in the frequency range of  $0.25 < a/\lambda < 0.30$ . From PWE simulations on optical mode profiles, we have confirmed that the two bandedges correspond with a dipole-like mode at  $a/\lambda \approx 0.29$  and a monopole-like mode at  $a/\lambda \approx 0.26$ , respectively. The corresponding each

mode profiles are shown in Figs. 2-2-1(b) and 2-2-1(c). By simply adjusting the lattice constant of PhCs, we could make the optical gain band of the InGaAsP MQWs match with either of the two bandedge modes: the dipole-like mode at a  $\approx 450$  nm and the monopole-like mode at a  $\approx 400$  nm.

The base wafer where the PhC BEL structure was to be formed was a standard InGaAsP MQW structure with the emission wavelength of  $\lambda \sim 1550$  nm. There are a 1- $\mu\text{m}$ -thick InP etch-sacrificial layer and an InGaAs etch-stop layer which are inserted underneath the MQW layer. The InP sacrificial layer has a high wet-etch selectivity over both for the InGaAsP MQW layer and InGaAs etch-stop layer, enabling to form an air-bridge MQW slab that serves as a waveguide along the wafer plane. A thin  $\text{Si}_3\text{N}_4$  layer deposited onto the base substrate served as a hard mask layer during the PhC pattern generation into the MQW slab by electron-beam lithography and reactive-ion-etching, sequentially. The  $\text{Si}_3\text{N}_4$  layer was removed afterwards and the InP etch-sacrificial layer was subsequently removed through the air-holes that formed the PhC pattern to finish the PhC BEL structure in the air-bridge format. Figures 2-2-1(d) and 2-2-1(e) show scanning electron microscope (SEM) images of a complete PhC BEL structure.

### 2.2.2 Device fabrication

The InGaAsP MQW structure was grown on an n-type (001)-oriented InP substrate by a low-pressure metal-organic chemical vapor deposition (CVD) system. Grown sequentially on the n-InP substrate were an InP buffer layer, a 50-nm-thick InGaAs etch-stop layer, 1000-nm-thick InP sacrificial layer, and finally 230-nm-thick MQW layer composed of five pairs of 8-nm-thick InGaAsP quantum well and 20-nm-thick InGaAsP barrier. Figure 2-2-2 shows schematic diagram of InGaAsP MQW structure. The entire PhC device fabrication process is as follows: A 50-nm-thick  $\text{Si}_3\text{N}_4$  hard mask layer was deposited on the InGaAsP MQW wafer by plasma-enhanced chemical vapor deposition (PECVD) at  $300^\circ\text{C}$ , followed by conventional electron-beam lithography to define a 2D honeycomb-lattice hole array pattern. The acceleration voltage and electron current during the pattern generation were 100 keV and  $300 \mu\text{C}/\text{cm}^2$ , respectively. Reactive-ion-etching (RIE) was then performed to transfer the PhC pattern into the hard mask layer and subsequently into the InGaAsP MQW layer, with the gas mixtures of  $\text{CF}_4/\text{O}_2$  for  $\text{Si}_3\text{N}_4$  and  $\text{CH}_4/\text{H}_2$  for InGaAsP, respectively. After removal of the remaining  $\text{Si}_3\text{N}_4$  hard mask layer with RIE, the sample was finally immersed in diluted HCl ( $\text{HCl}:\text{H}_2\text{O} = 3:1$ ) to remove selectively the InP sacrificial layer underneath the MQW layer, which resulted in the air-bridge PhC nanolaser.

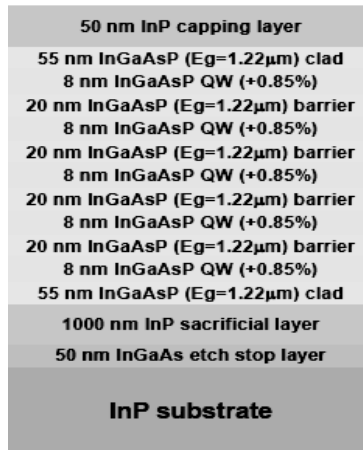


Fig. 2-2-2 Schematic diagram of InGaAsP MQW structure.

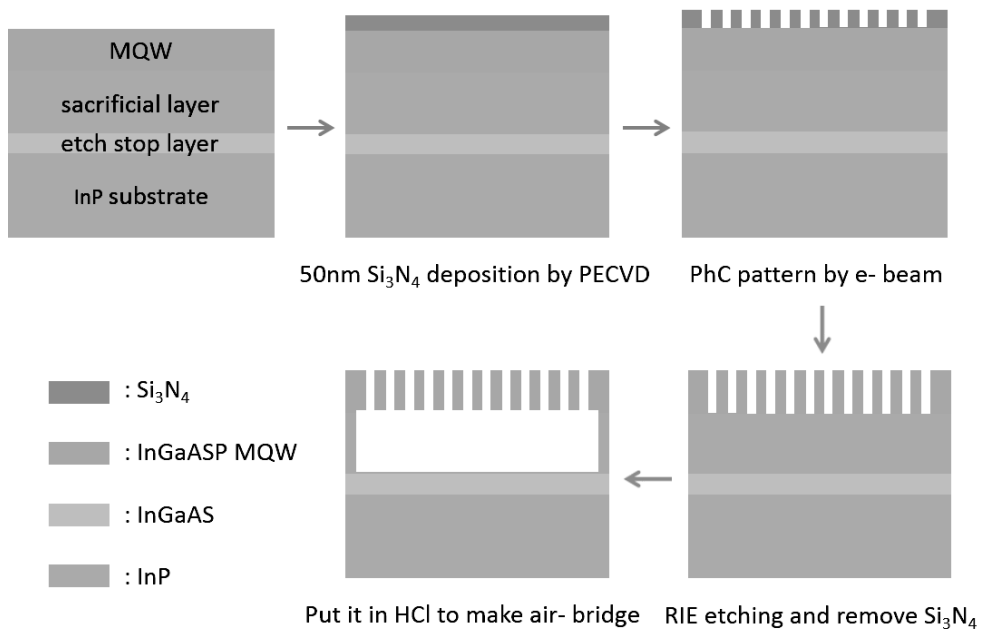


Fig. 2-2-3 Fabrication processes of PhC bandedge laser.

## 2.3 ALD surface passivation

### 2.3.1 Atomic layer deposition

Our air-bridge BEL structure with a 2D array of air-holes has a high surface-to-volume ratio (SVR), so it is suitable for biochemical sensing application where a strong overlap between the optical resonance mode and the external environmental medium is highly desirable. However, a high SVR implies inevitable exposure of a substantial semiconductor surface area. Therefore, surface protection would be appropriate to keep the BEL device from disruptive environmental substances that may be encountered for various reasons; it is worth mentioning that the InP-based semiconductor materials are known to be readily dissolved in many chemicals [20]. In addition, exposed surfaces inevitably induce a large number of dangling bonds and related extrinsic defects, which usually act as non-radiative surface recombination centers that result in rapid carrier annihilation [21]. Therefore, a certain form of surface passivation should be required for both short-term and long-term BEL device performances.

A variety of surface passivation methods have been developed for compound semiconductor based photonic devices. Among others, thin film deposition provides physically more secure and stable means of device protection. However, the deposited layer should remain very thin in order not to ruin the virtue of strong overlap between optical mode and outer medium, a crucial condition for high sensitivity in biochemical sensing. Here, we employed ALD technique to coat the entire surface of an air-bridge InGaAsP MQW PhC BEL with a uniform and conformal layer of only a few nm-thick SiO<sub>2</sub> film. The ALD is a thin film deposition technique that utilizes chemical adsorption and substitution of molecules to deposit an atomically thin film layer. It is particularly useful to deposit a uniform film on all sides and corners of sample to the thickness of ~nm, regardless of the shape of substrate: gas phase material sources can reach even every corner and face that would be inaccessible with

any physical deposition technique. When applied to our PhC laser structure, the ALD process allows gas molecules to reach even the underneath surface of the air-bridge membrane through the open air-holes that constitute the PhC pattern, resulting in a uniform passivation layer deposited not only on the top surface but also on the sidewalls as well as the bottom face of the MQW slab, yet with nanometer precision in film thickness.

### 2.3.2 ALD-SiO<sub>2</sub> passivation procedure

Silicon oxide films were deposited by the ALD process on the honeycomb-lattice two dimensional photonic crystal structure. Two precursors, trimethylaluminum (TMA) and tri(*tert*-butoxy)silanol, were sequentially pulsed through the reaction chamber. First, TMA was pulsed into the chamber for 0.15 secs followed by an N<sub>2</sub> carrier gas with flow rate 20 sccm for 5 sec to remove the TMA from the chamber. Second, silanol was pulsed into the chamber and allowed to react for 30 sec, followed by the N<sub>2</sub> carrier gas with flow rate 20 sccm for 30 sec to remove the silanol from the chamber. This sequence was repeated for each cycle of SiO<sub>2</sub> deposition. The operating temperature was 250 °C for depositing SiO<sub>2</sub> layer on InGaAsP MQW. This is an adaptation from Hausmann et al, Science, 2005 [22]. The deposition rate was around 1 nm SiO<sub>2</sub> per cycle. The samples were coated with roughly 4, 9, and 15 nm, as measured by ellipsometry.

### 2.3.3 ALD-SiO<sub>2</sub> passivation layer on the performance of PhC BEL

The purpose of the following experiments is to make sure that the ALD-SiO<sub>2</sub> thin film can protect well the entire surface from harsh environment. At first, a SiO<sub>2</sub> thin film was deposited on an InP bare wafer by the ALD process, following the procedure described by Im *et al.* [23]. We controlled the deposition time to obtain a desired film thickness of ~nm, knowing the deposition rate for the given deposition conditions that is pre-calibrated with a much thicker film. Figure 2-3-1 shows a transmission electron microscope (TEM) image taken for a nominally 5-nm-thick ALD-SiO<sub>2</sub> film, direct visual evidence that a few nm thick dielectric film was truly deposited. To test its durability and ability to protect the bare InP substrate, we defined an circular photoresist patterns of 400 μm in diameter by using conventional photolithography. A sample prepared was immersed in buffered oxide etchant (BOE) for 20 sec to remove the ALD-SiO<sub>2</sub> film from the regions uncovered with photoresist, which was followed by photoresist stripping in acetone. The sample was then intentionally soaked for 30 sec in dilute HCl solution (HCl: H<sub>2</sub>O = 3:1), which is known to be a very efficient InP etchant. Shown in Fig. 2-3-2 is an SEM image for a circular mesa that was formed after the HCl etch. The InP substrate where the ALD-SiO<sub>2</sub> layer was absent was etched severely to a depth of ~3 μm in the region, whereas the circular region defined and passivated by the ALD-SiO<sub>2</sub> layer perfectly undamaged. This is true evidence that the ALD-SiO<sub>2</sub> film protects the InP substrate even from extremely harsh environments, despite its diminishingly negligible thickness.

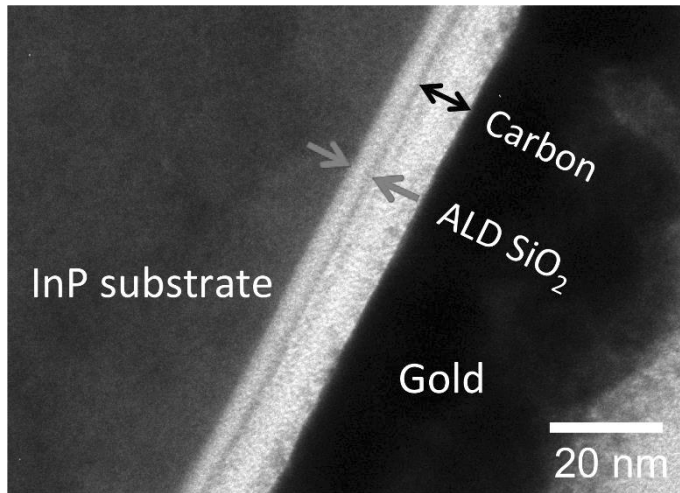


Fig. 2-3-1 Cross-sectional TEM image of an ALD-SiO<sub>2</sub> layer deposited on an InP bare substrate.

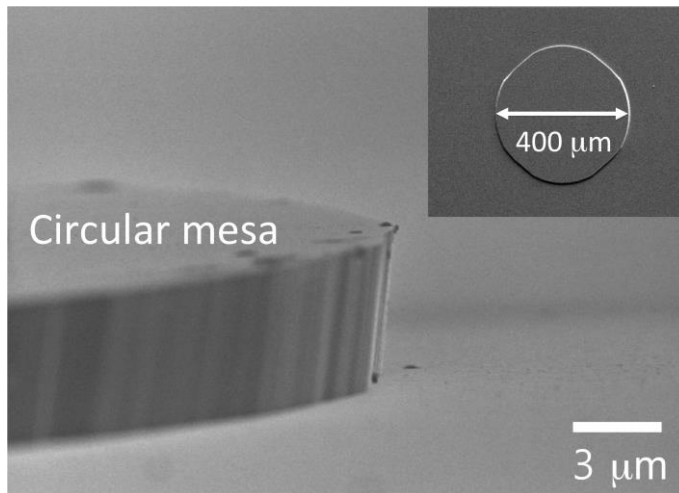


Fig. 2-3-2 SEM image of an InP circular mesa etched in a diluted HCl solution with the mesa top protected by the ALD-SiO<sub>2</sub> layer. Inset is another SEM image of the circular mesa taken from the top.

Successful result from the initial test on the bare InP substrate, we finally applied the ALD-SiO<sub>2</sub> passivation to our PhC bandedge laser device. A 5-nm-thick SiO<sub>2</sub> film was deposited onto the air-bridge  $\Gamma$ -point BEL structure. Then, we immersed the sample in piranha solution (H<sub>2</sub>SO<sub>4</sub>: H<sub>2</sub>O<sub>2</sub>: H<sub>2</sub>O = 1:1:10) for two minutes, which are strong and long enough to completely etch out the thin InGaAsP MQW layer unless the ALD-SiO<sub>2</sub> layer efficiently protects the InGaAsP material from the etchant. With the optical microscope, it revealed that the PhC BEL devices remained intact after the etch trial, with the air-bridge membrane structure unchanged from its initial shape. With the visual test, we operated the PhC BELs to examine their lasing performance characteristics. Both BEL devices were pumped using 980 nm pulsed laser diode (20 ns pulse width and 1% duty cycle), and optical emission from the device was fed into an optical spectrum analyzer. In this experiment, we used micro-photoluminescence (PL) setup which employs the combination of a butt-end fiber tip and a 1x2 wavelength division multiplexing (WDM) fiber coupler for measurement with the advantage of alignment. This is capable of doing optical pumping and collecting the emission of light simultaneously. Figure 2-3-3 is a schematic diagram of fiber based micro-PL setup [19]. Figure 2-3-4 shows lasing spectra of a typical BEL device recorded at different sample treatment stages such as fabricated, after ALD-SiO<sub>2</sub> layer deposition, and after 2 mins treatment in piranha solution. While the ALD-SiO<sub>2</sub> layer deposition caused a sizable redshift ( $\Delta\lambda \sim 8.7$  nm) in lasing peak position, which was due to the increase in the effective refractive index of device, the subsequent 2 mins piranha solution treatment gave absolutely no effect to lasing peak position. This result is strong evidence that the 5-nm-thick ALD-SiO<sub>2</sub> layer provides an almost perfect means of device protection from harsh chemicals. We also noticed that the BEL devices performed even better after the ALD-SiO<sub>2</sub> layer deposition, as shown in

Fig. 2-3-5: lasing threshold becomes lower by ~30% while slope efficiency is enhanced more than two times. We believe that these results are due to a partial remedy of dangling bonds by the ALD process, which in turn leads to the reduction of non-radiative recombination centers. Detailed mechanisms for the improved laser performance are subject to a further study in the future.

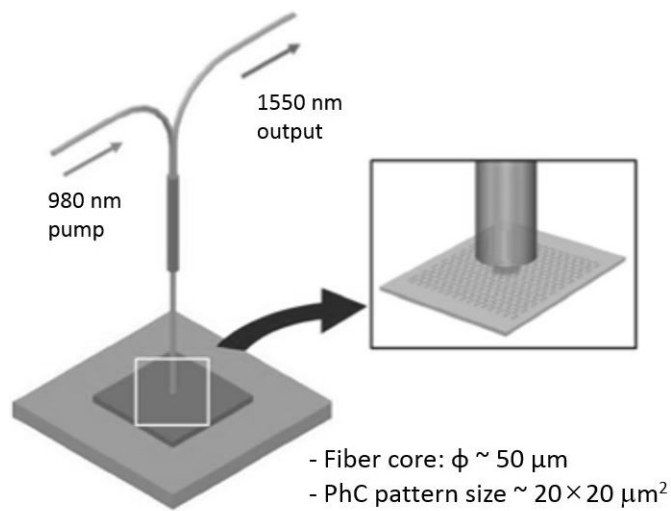


Figure 2-3-3 Schematic diagram of fiber based micro-PL setup [19].

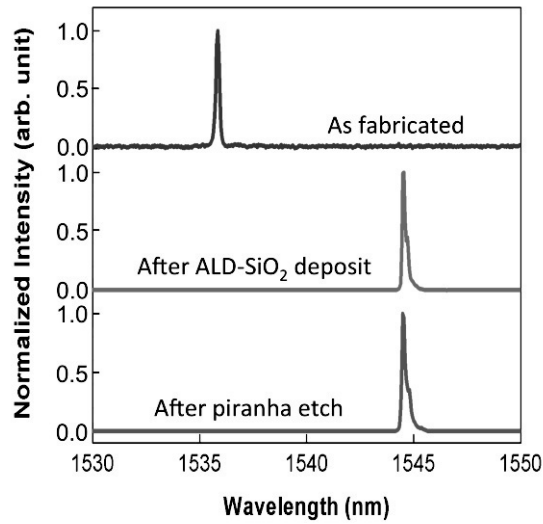


Figure 2-3-4 Lasing spectra from an InGaAsP MQW BEL device, taken at different stages of sample treatments.

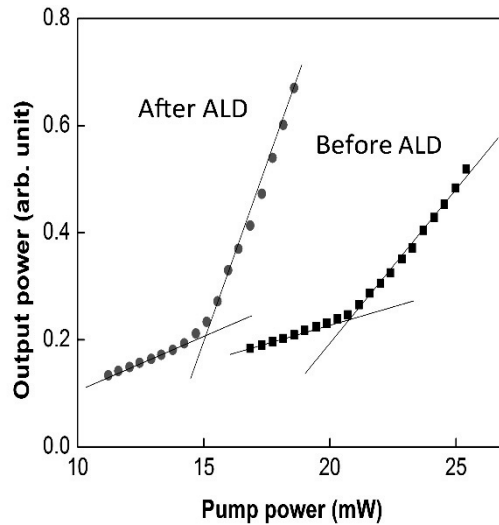


Figure 2-3-5 Input power vs. output power relations of a typical BEL device.

## 2.4 Biosensing results and discussion

### 2.4.1 Biosensing preparation with streptavidin-biotin interaction

We investigated the possibility of using the PhC BEL devices passivated with ALD-SiO<sub>2</sub> for biosensing application. Many label-free biosensing devices rely on the surface interaction between two kinds of molecules, ligands and receptors, and should therefore respond to the ligand-receptor interaction sensitively enough to cause a noticeable change in detection signal. For that matter, devices based on nanophotonics principles are attractive candidates because they offer a large signal change due to their strong field enhancement effect at spatially localized spots or regions as well as their large SVR. On the other hand, biosensing devices often undergo treatments or preparation steps that involve various chemicals, part of which may be harsh enough to damage or destroy the small sized devices. Conformal deposition of a surface passivation layer is therefore an appropriate approach for device protection. The passivation layer however needs to be very thin if one wants to fully exploit the local field enhancement effect of nanophotonic devices. The ALD process satisfies the both conditions described above; it can coat every exposed surfaces regardless of the shape and configuration of device, and yet it can control the thickness down to ~nm. It should be noted that we employed an ALD-SiO<sub>2</sub> layer, not an ALD-Al<sub>2</sub>O<sub>3</sub> layer in this study. In fact, we intentionally chose the ALD-SiO<sub>2</sub> because the silane-based chemistry, which has been developed for a hydroxyl group-terminated surface to full maturity, can be readily used without any extra surface preparation process.

We performed biosensing experiments using standard streptavidin-biotin interaction, which is known to form the strongest non-covalent complex between protein and ligand (dissociation constant:  $K_d = 10^{-15}$  M), and is hardly affected by experimental circumstances, such as pH, organic solvents, temperature, and other agents. Due to these bonding natures, the complex has been used in many protein and

nucleic acid detection and purification methods [24,25].

The overall surface functionalization procedure for biosensing experiment is detailed as follows: In order to have the streptavidin-biotin interaction occur on the PhC BEL device, we first passivated an array of PhC BEL devices with a nominally 5-nm-thick ALD-SiO<sub>2</sub> layer. Prior to a series of surface chemistry, the sample had gone through standard solvent cleaning procedure and treated in piranha solution afterwards, which should remove any organic residue on the SiO<sub>2</sub>-terminated device surface. The sample was then left soaked overnight in 2% solution of (3-aminopropyl) triethoxysilane (APTES) in phosphate buffered saline (PBS) solution, which resulted in the ALD-SiO<sub>2</sub> terminated sample surface covered with a monolayer of APTES molecules via self-assembled monolayer (SAM) process. The APTES molecules, known as a coupling agent, make the SiO<sub>2</sub> surface more favorable to biotin molecules; it is widely used in biological implant, such as protein adhesion and cell growth. After the APTES treatment, the sample was incubated about 3-4 hours in the mixture solution of NHS (*N*-hydroxysuccinimide) esters of polyethylene glycol (PEG) and biotin-PEG in 100 mM sodium bicarbonate buffer (pH 8.25) to prepare a partially biotin-terminated surface. It should be noted that the rest of the surface is simply PEG-terminated, which prevents non-specific binding of protein like streptavidin, so the streptavidin binds selectively to biotin-terminated surface only. We controlled the relative concentrations between PEG and biotin-PEG such that biotin covers ~10 % of the total surface area. A drop of 100 nM streptavidin conjugated with R-phycoerythrin fluorescence dye (SAPE) was released on the biotin-PEG terminated sample to induce the streptavidin-biotin interaction. We intentionally utilized the dye conjugated streptavidin so that we could visually confirm the streptavidin-biotin interaction. Finally, the sample was rinsed in deionized water and dried. The overall sample preparation procedure is schematically outlined in Fig. 2-4-1. One thing we should note that although our device should work as a label-free sensor, we intentionally attached fluorescing dye molecules to streptavidin so that we could

monitor and confirm the streptavidin-biotin interaction with fluorescence microscopy as well. In fact, we captured fluorescence image of the sample after biofunctionalization, which is shown in Fig. 2-4-2, and found that the PhC patterned area, filled with air-holes and thus having a high SVR, exhibited fluorescence intensity much stronger than the planar region without any PhC pattern. This result confirms that the overall surface chemistry was properly accomplished.

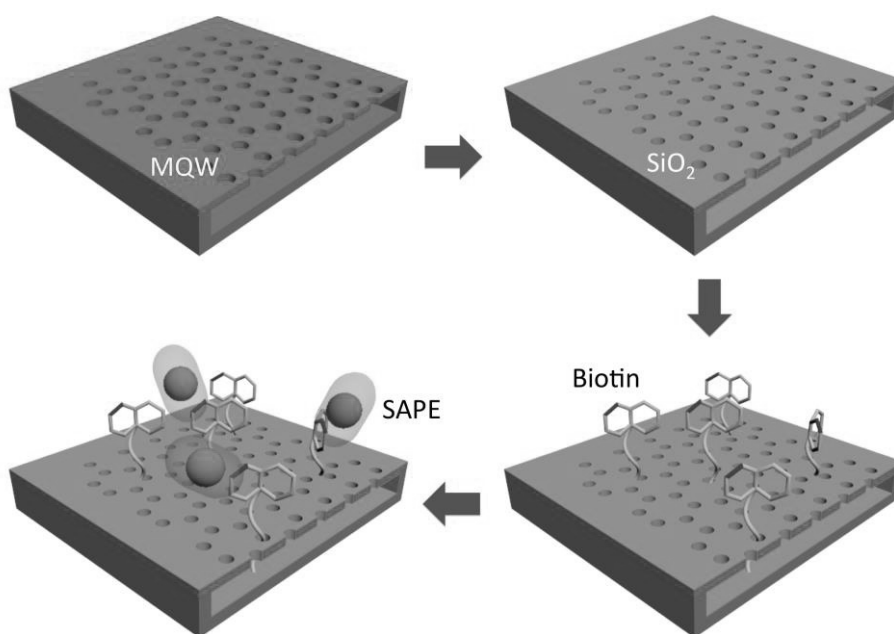


Figure 2-4-1 Schematic diagram of surface functionalization steps for biosensing test. From the top, 2D PhC BEL fabrication; conformal deposition of an ALD- $\text{SiO}_2$  layer; biotinylation on the silica-terminated surface; and the interaction between biotin and streptavidin molecules tagged with fluorescence dye (SAPE).

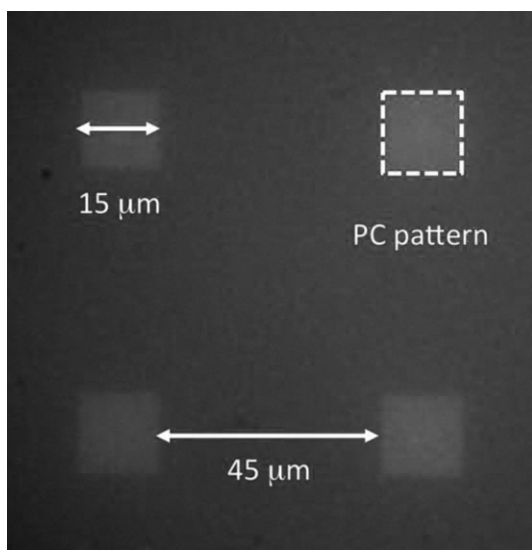


Figure 2-4-2 Fluorescence microscopy image taken after the streptavidin-biotin interaction.

## 2.4.2 Measurement

Lasing spectra of the ALD-SiO<sub>2</sub> passivated PhC BELs were measured before and after the streptavidin-biotin interaction process. Shown in Fig. 2-4-3 is typical lasing spectra before and after the streptavidin-biotin interaction for both the dipole-like and monopole-like BEL modes. It is clear from the figure that the BEL peaks shifted by  $\sim 0.95$  nm for the dipole-like mode and by  $\sim 0.80$  nm for the monopole-like mode, respectively; similar spectral redshifts was consistently measured throughout all the BEL devices in the same batch. The measured results indicate that our PhC BELs are quite competitive when compared with other nanophotonics based sensors. For example, it was reported that plasmonic resonance from an 10% biotinylated Ag nanohole array redshifted by  $\sim 1.3$  nm with 100 nM SAPE [26]; although the sensing mechanisms are quite different, the amounts of resonance shift are in the same order, inferring similar sensitivities. It is worth mentioning that the spectral peak shift for the dipole-like mode was slightly larger than that for the monopole-like mode; we attribute this to the fact that the dipole-like mode is a little bit larger and consequently its electric field extends further into the air-holes, which makes the dipole-like mode respond to the environmental change more strongly, leading to a higher sensitivity [27].

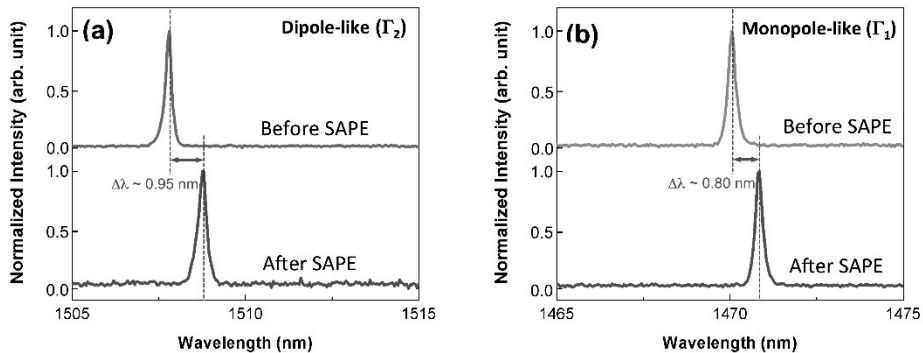


Figure 2-4-3 Lasing spectra of positively controlled BEL biosensors before and after the streptavidin-biotin interaction: (a) dipole-like mode and (b) monopole-like mode.

We also prepared and counter-checked a negative-control sample, for which the biotin-PEG process was intentionally done with bare PEG so that the streptavidin-biotin interaction could not occur from the beginning, leaving the full surface free of any intentional streptavidin-biotin molecules. In good contrast, the negative-control sample exhibited no spectral shift for the both types of bandedge modes which is less than 0.05 nm, that is the resolution limit in our optical spectrum analyzer that we used for the measurement as shown in Fig. 2-4-4. By taking the ratio of the peak shifts between the positive- and negative-control samples, we obtain the a signal-to-noise ratio (SNR) greater than 20 for the dipole-like mode, which is large enough to be sure that the streptavidin-biotin interaction is detected.

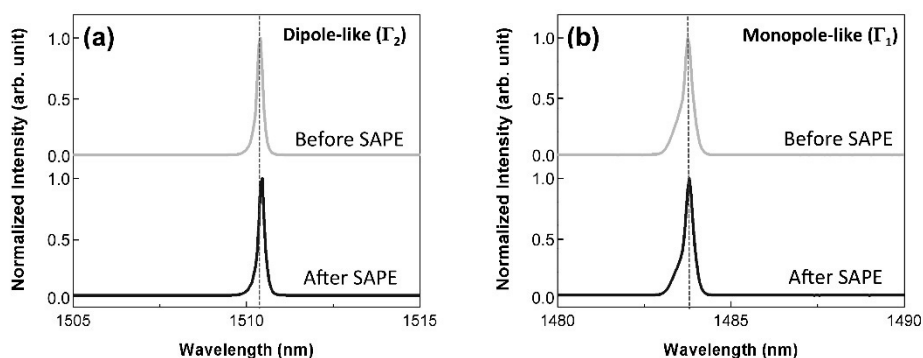


Figure 2-4-4 Lasing spectra of negatively controlled (biotin-free) BEL biosensors before and after the streptavidin treatment: (a) dipole-like mode and (b) monopole-like mode.

We performed band structure calculations for our honeycomb-lattice 2D PhC structure to estimate how fast the bandedge shifts as the refractive index of the environmental medium changes. From the calculations, we estimated the index sensitivity to be  $\sim 163$  nm/RIU (RIU: refractive index unit) for the dipole-like mode. A common parameter used to quantify the quality of a biosensor is the figure-of-merit

(FOM), which is defined as the wavelength shift per unit refractive index change divided by the linewidth of the resonance peak at its full-width at half-maximum. The FOM of our dipole-like BEL mode turns out to be  $\sim 800$ , when the typical linewidth of our BEL lasing peak of  $\sim 0.2$  nm is taken. This FOM value is huge in comparison with typical FOMs of the conventional sensors that rely on a broad resonance peak, such as surface plasmon resonance [28,29]. Combining all the virtues of our  $\Gamma$ -point BEL sensors, such as a huge FOM value, high output power, vertical emission, and relaxed alignment tolerance (due to the infinite translational symmetry of a BEL pattern structure), it should be greatly facilitated to simplify the sensing procedure and miniaturize the sensing system.

## 2.5 Summary

We fabricated air-bridge type 2D PhC BELs using an InGaAsP MQW structure and subsequently applied the ALD process to passivate the entire device surface with a few nm-thick conformal SiO<sub>2</sub> layer. Despite the extreme thickness, the ALD-SiO<sub>2</sub> layer was found to protect the devices almost perfectly from harsh chemical environments and also to improve lasing performance. The ALD-SiO<sub>2</sub> passivated BEL devices were tested as a biosensor by employing standard streptavidin-biotin interaction. Therefore, we obtained the figure-of-merit of the sensor to be ~800, which is at least an order of magnitude higher when compared with the conventional SPR-based sensors. Such a large FOM is due to a sharp resonance peak, which is enabled by lasing action at the resonance. Together with virtues of the  $\Gamma$ -point BEL, high output power emitted in the direction normal to the device surface, these preliminary test results brighten the way to a compact and ultrasensitive biosensor platform based on nanophotonics technology.

## References

- [1] N. V. Lavrik, M. J. B. Sepaniak, and P. G. Datskos, "Cantilever transducers as a platform for chemical and biological sensors," *Review of Scientific Instruments*, **75**, 2229-2253, (2004).
- [2] F. Josse, F. Bender, and R. W. Cernosek, "Guided shear horizontal surface acoustic wave sensors for chemical and biochemical detection in liquids," *Analytical Chemistry*, **73**, 5937-5944, (2001).
- [3] E. Braun, and K. Keren, "From DNA to transistors," *Advances in Physics*, **53**, 441-496, (2004).
- [4] Y. Cui, Q. Wei, H. Park, and C. M. Lieber. "Nanowire nanosensors for highly sensitive and selective detection of biological and chemical species," *Science*, **293**, 1289-1292, (2001).
- [5] H. Im, X. J. Huang, B. Gu, and Y. K. Choi, "A dielectric-modulated field-effect transistor for biosensing," *Nature Nanotechnology*, **2**, 430-434, (2007).
- [6] C. L. Feng, X. H. Zhong, M. Steinhart, A. M. Caminade, J. P. Majoral, and W. Knoll, "Graded-bandgap quantum-dot-modified nanotubes: A sensitive biosensor for enhanced detection of DNA hybridization," *Advanced Materials*, **19**, 1933-1936, (2007).
- [7] T. J. Kippenberg, S. M. Spilane, D. K. Armani, and K. J. Vahala, "Fabrication and coupling to planar high-Q silica disk microcavities," *Applied Physics Letter*, **83**, 797-799, (2003).
- [8] I. M. White, H. Zhu, J. D. Suter, N. M. Hanumegowda, H. Oveys, M. Zourob, and X. Fan, "Refractometric Sensors for Lab-on-a-Chip Based on Optical Ring

- Resonators,” *IEEE Sensors Journal*, **7**, 28-35, (2007).
- [9] W. Liang, Y. Huang, Y. Xu, R. K. Lee, and A. Yariv, “Highly sensitive fiber Bragg grating refractive index sensor,” *Applied Physics Letters*, **86**, 151122, (2005).
- [10] M. L. Adams, M. Loncar, A. Scherer, and Y. Qiu, “Microfluidic integration of porous photonic crystal nanolasers for chemical sensing,” *IEEE Journal on Selected Areas in Communications*, **23**, 11348-1354, (2005).
- [11] S. Kita, K. Nozaki, and T. Baba, “Refractive index sensing utilizing a cw photonic crystal nanolaser and its array configuration,” *Optics Express*, **16**, 8174-8180, (2008).
- [12] S. Kita, S. Otsuka, S. Hachuda, T. Endo, Y. Imai, Y. Nishijima, H. Misawa, and T. Baba. “Photonic crystal nanolaser biosensors,” *IEICE Transactions on Electronics*, **95**, 188-198, (2012).
- [13] E. M. Larsson, S. Syrenova, and C. Langhammer, “Nanoplasmonic sensing for nanomaterials science.” *Nanophotonics*, **1**, 249-266, (2012).
- [14] F. H. Ho, Y. H. Wu, M. Ujihara, and T. Imae, “A solution-based nano-plasmonic sensing technique by using gold nanorods,” *Analyst*, **137**, 2545-2548, (2012).
- [15] D. J. Norris, “Photonic crystals: A view of the future,” *Nature Materials*, **6**, 177-178, (2007).
- [16] T. Baba, “Slow light in photonic crystals,” *Nature Photonics*, **2**, 465-473, (2008).
- [17] H. G. Park, S. H. Kim, S. H. Kwon, Y. G. Ju, J. K. Yang, J. H. Baek, S. B. Kim, and Y. H. Lee, “Electrically driven single-cell photonic crystal laser,” *Science*, **305**, 1444-1447, (2004).
- [18] S. Kim, J. Lee, and H. Jeon, “Over 1 hour continuous-wave operation of photonic

- crystal lasers,” *Optics Express*, **19**, 1-6, (2011).
- [19] S. Kim, Y. Park, K. Hwang, J. Lee, H. Jeon, and H. J. Kim, “High-power and large-alignment-tolerance fiber coupling of honeycomb-lattice photonic crystal  $\Gamma$ -point band-edge laser,” *Journal of the Optical Society of America B*, **26**, 1330-1333, (2009).
- [20] P. H. Holloway and D. E. McGuire, *Handbook of Compound Semiconductors* (William Andrew Inc. 1996).
- [21] P.T. Landsberg, *Recombination in semiconductors*, (Cambridge University Press 1991).
- [22] D. Hausmann, J. Becker, S. Wang, and R. G. Gordon, “Rapid vapor deposition of highly conformal silica nanolaminates,” *Science*, **298**, 402-406, (2002).
- [23] H. Im, N. C. Lindquist, A. Lesuffleur, and S. H. Oh, “Atomic layer deposition of dielectric overlayers for enhancing the optical properties and chemical stability of plasmonic nanoholes,” *ACS Nano*, **4**, 947-954, (2010).
- [24] M. D. Savage, *A Laboratory Guide to Biotin-labeling in Biomolecule Analysis*, pp.1-29 (Birkhäuser Verlag Basel 1996).
- [25] N. M. Green, “Avidin. 3. The nature of the biotin-binding site,” *Biochemical Journal*, **89**, 599-609, (1963).
- [26] H. Im, S. H. Lee, N. J. Wittenberg, T. W. Johnson, N. C. Lindquist, P. Nagpal, D. J. Norris, and S. H. Oh, “Template-stripped smooth Ag nanohole arrays with silica shells for surface plasmon resonance biosensing,” *ACS Nano*, **8**, 6244-6253, (2011).
- [27] S. Kim, J. Lee, H. Jeon, and H. J. Kim, “Fiber-coupled surface-emitting photonic

crystal band edge laser for biochemical sensor applications,” *Applied Physics Letters*, **94**, 133503, (2009).

[28] Y. Shen, J. Zhou, T. Liu, Y. Tao, R. Jiang, M. Liu, G. Xiao, J. Zhu, Z. K Zhou, X. Wang, C. Jin, J. Wang, “Plasmonic gold mushroom arrays with refractive index sensing figures of merit approaching the theoretical limit,” *Nature Communications*, **4**,1-9 (2013).

[29] A. A. Yanik, M. Huang, A. Artar, T. Y. Chang, H. Altug, H. Im, N. C. Lindquist, A. Lesuffleur, and S. H. Oh, in *Plasmonics: Metallic Nanostructures and Their Optical Properties VIII*, Vol. 7757 (Eds: M. I. stockman), SPIE, San Diego, California, USA 2010, pp. 775735–1–6.



# Chapter 3

## Two-dimensional photonic crystal bandedge laser with hybrid perovskite thin film for optical gain

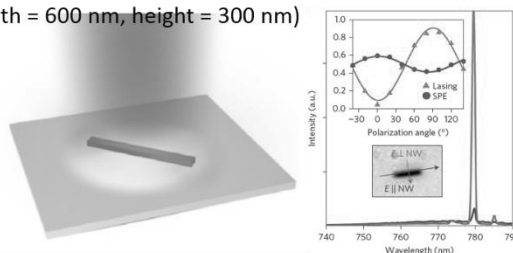
### 3.1 Introduction

During the past few years, organic-inorganic lead halide perovskite has been demonstrated to be an alternative light harvester with great power conversion efficiency (PCE) in photovoltaics research area. In the hybrid perovskite materials, methyl-ammonium lead iodide ( $\text{CH}_3\text{NH}_3\text{PbI}_3$ ) which is most commonly represented have drawn tremendous attentions lately due to their high potential for photovoltaics application; long carrier lifetimes and diffusion lengths [1-3], high internal quantum efficiency [4,5], and stoichiometric wavelength tenability [6] are a few virtues of the material system. Firstly, Kojima et al. demonstrated photovoltaic cells (PVCs) employing the hybrid perovskites as light absorber; the power conversion efficiency approached about 4% [7], and the PCE of the hybrid perovskite PVCs has now exceeded 20% [8].

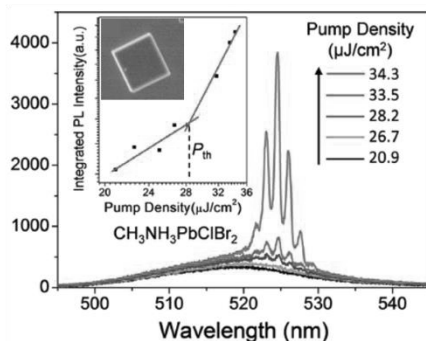
Such a high PVC performance shows that the hybrid perovskites are promising light-absorbing materials [9-11], which in turn infers that they could also act as efficient light emitters when electron-hole pairs are properly generated within them. In fact, optically pumped lasing actions have been demonstrated from the hybrid perovskite materials with various cavity geometries shown in Fig. 3-1-1, which include nanowires [12], microdisks [13], nanoplatelet [14], and random networks [15]. However, these laser structures intrinsically support multiple laser modes, so it cannot

guarantee single mode laser operation, which is a crucially important property for sophisticated photonic information technologies such as optical communications and computing. Here, we report room-temperature single mode lasers based on hybrid perovskite material, methylammonium lead iodide ( $\text{CH}_3\text{NH}_3\text{PbI}_3$ ), as gain material, in which single mode operation is enabled by a photonic bandedge mode supported by two-dimensional (2D) photonic crystal (PhC) structure with square lattice.

Single nanowire with a length of  $8.5\ \mu\text{m}$   
(width =  $600\ \text{nm}$ , height =  $300\ \text{nm}$ )



Single square microdisk with width =  $6.2\ \mu\text{m}$



Hexagonal nanoplatelet (thickness =  $150\ \text{nm}$ , length =  $32\ \mu\text{m}$ )

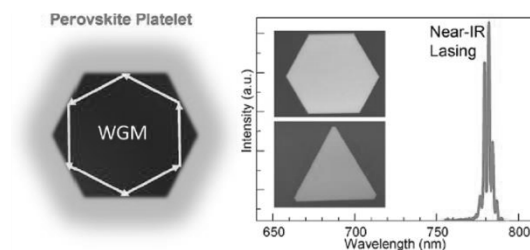


Figure 3-1-1 Halide perovskite materials for photonic applications with various cavity geometries. [12-14]

## 3.2 2D square lattice photonic crystal bandedge laser

### 3.2.1 Photonic crystal bandedge mode

Photonic bandedge modes, which are typically established on both edges of a photonic bandgap at high symmetry points in the momentum space, are characterized by a periodically bunched stationary field profile, whose nodes and antinodes are related to the corresponding PhC lattice. When a bandedge mode is resonantly tuned with the energy of emitted photons from gain material, which is typically a part of PhC structure, it can lase. So far, various types of bandedge lasers have been demonstrated using different PhC structures and materials [16-18]. In particular, 2D PhC bandedge lasers employing a  $\Gamma$ -point bandedge mode have an interesting property; they emit a stimulated emission in the vertical direction even optical feedback for lasing action occurs along the 2D PhC plane. In our research group, we have achieved a few significant things in bandedge laser research: high fiber-coupled output power (in mW level) as well as a long device lifetime (up to 18 hours) under continuous-wave (CW) operation condition, using InGaAsP-based multiple quantum well structures [19,20].

### 3.2.2 Device fabrication

Overall device structure of  $\text{CH}_3\text{NH}_3\text{PbI}_3$  PhC bandedge laser is schematically shown in Fig. 3-2-1(a). There are two independent and parallel tasks involved for sample preparation. One is a preparation of a hybrid perovskite as active medium, and the other is fabrication of 2D photonic crystal square lattice backbone structure. As for the perovskite material, methylammonium iodide ( $\text{CH}_3\text{NH}_3\text{I}$ ) was synthesized by reacting equimolar methylamine (40% in methanol, TCI) with hydroiodic acid (HI, Alfa Aesar, 57% w/w aqueous solution stabilized with 1.5% hypophosphorous acid) at 0 °C. HI was added dropwise to methylamine solution under constant stirring. After a reaction time of 2 hours, solvent was evaporated using a rotary evaporator and the product was recrystallized from ethanol and diethyl ether. After filtration, the precipitate was washed with diethyl ether and dried at 60 °C in vacuum oven for 24 hours. Lead iodide ( $\text{PbI}_2$ , Acros Organics, 99%) was dried in vacuum oven at 240 °C for 12 hours. To prepare the perovskite precursor solution, 1.18 mmol of  $\text{CH}_3\text{NH}_3\text{I}$  with equimolar  $\text{PbI}_2$  were dissolved in 1 mL of dimethyl sulfoxide (DMSO) [21].

On the other hand, the fabrication of the PhC square lattice backbone structure began with a sequential layer depositions of  $\text{SiO}_2$  and  $\text{Si}_3\text{N}_4$  on silicon wafer by plasma-enhanced chemical vapor deposition (PECVD). The thicknesses of each layer were 1  $\mu\text{m}$  for  $\text{SiO}_2$  and 140 nm for  $\text{Si}_3\text{N}_4$ , respectively. An array of square lattice air-hole patterns was generated by conventional electron-beam lithography technique. Subsequent pattern transfer down to the  $\text{Si}_3\text{N}_4$  layer was accomplished by a selective reactive-ion etch (RIE); for this purpose, we used the RIE recipe which is added  $\text{N}_2$  to the standard RIE gas mixture of  $\text{CF}_4$  and  $\text{O}_2$  to improve the etch selectivity of  $\text{Si}_3\text{N}_4$  over  $\text{SiO}_2$  [22]. This  $\text{SiO}_2$  layer simply serves an optical cladding while the PhC-engraved  $\text{Si}_3\text{N}_4$  layer constitutes a lateral waveguide along with a perovskite film that

is spin-coated atop later. Figures 3-2-1(b) and (c) show scanning electron microscope (SEM) images taken from a fabricated PhC backbone structure.

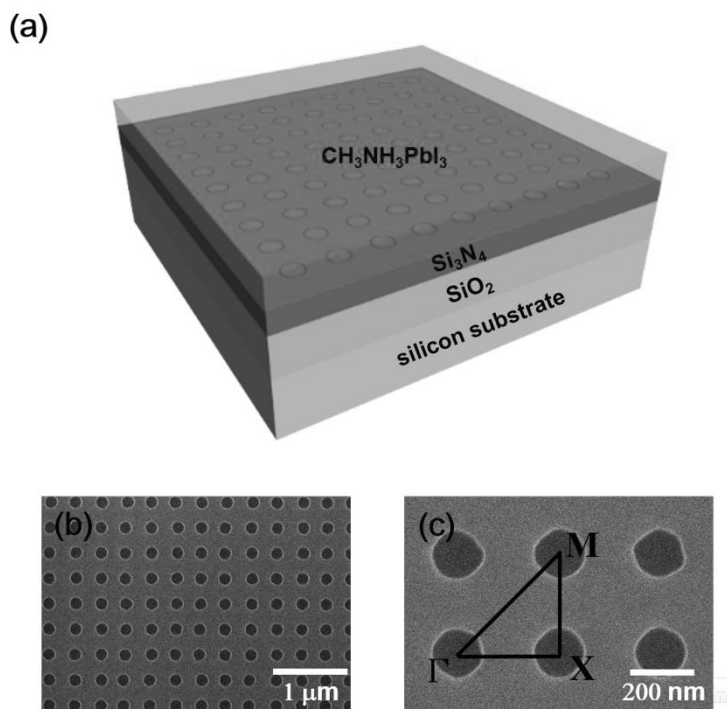


Figure 3-2-1 (a) Schematic of the CH<sub>3</sub>NH<sub>3</sub>PbI<sub>3</sub> PhC bandedge laser structure. (b) SEM image of the square lattice PhC backbone, fabricated on the Si<sub>3</sub>N<sub>4</sub> layer with (b) low and (c) high magnifications. The SEM images are from gamma point bandedge laser sample:  $a_{\Gamma} = 345$  nm and  $\phi_{\Gamma} = 150$  nm. A reciprocal lattice of square lattice is schematically drawn in (c).

The substrate containing the 2D square lattice PhC pattern was treated with UV-ozone for 15 mins and then immediately transferred to N<sub>2</sub>-filled glovebox. DMSO perovskite precursor solution was spin-coated at 3000 rpm for 60 sec on the substrate. During the spin-coating, 0.2 mL of diethyl ether was dropped on the film after 45 sec

to extract excess DMSO and the substrate was immediately transferred on a hot plate at 110 °C for 2 mins for crystallization of perovskite material. The overall PhC bandedge laser preparation procedure is schematically outlined in Fig. 3-2-2.

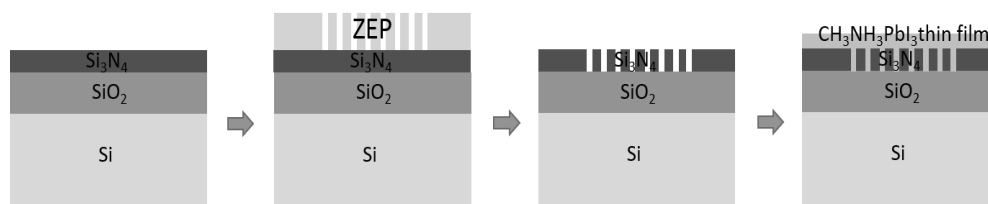


Figure 3-2-2 Fabrication processes of PhC bandedge laser with perovskite thin film.

Shown in Figs. 3-2-3(a) and (b) are optical microscope images taken before and after the deposition of perovskite film, which confirms that the perovskite film coating was accomplished uniformly. The checkerboard pattern shown in the figures is intentionally inserted to facilitate the location and identification of individual PhC patterns. Although it looks quite homogeneous and uniform over the entire pattern under optical microscope, SEM image shows that the surface morphology of the hybrid perovskite film is far from perfection—Fig. 3-2-3(c). From the separate atomic force microscope (AFM) measurement, we obtained the root-mean-square (RMS) value of surface roughness is about 45 nm. It should be noted that we controlled spin-coating and baking time tightly in order to minimize the formation of pinholes, a well-known problem with one-step deposition of perovskite films. Figure 3-2-3(c) indicates that the quality of perovskite film should be still improved substantially. However, with this roughness of perovskite thin film, resultant devices lased out as we will explain this happen later. Therefore, there is much room for the improvement in laser performance. Figure 3-2-3(d) is a cross-sectional SEM image for a local area where the PhC pattern is partially exposed. One can see that the roughness of the

crystallized  $\text{CH}_3\text{NH}_3\text{PbI}_3$  film surface again. Nevertheless, the SEM image confirms that the perovskite material is properly infiltrated into the PhC air-holes formed in the  $\text{Si}_3\text{N}_4$  layer.

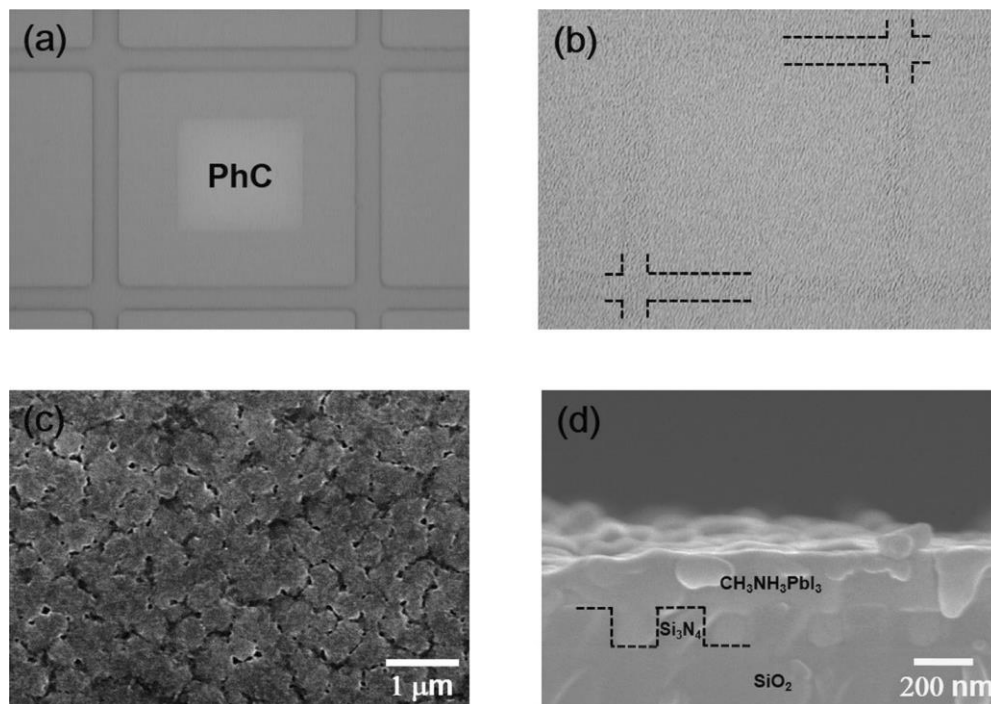


Figure 3-2-3 Optical microscope images taken (a) before and (b) after the deposition of  $\text{CH}_3\text{NH}_3\text{PbI}_3$  thin film. In (a), the bright square region in the middle corresponds to the PhC patterned area. SEM images of a fully fabricated  $\text{CH}_3\text{NH}_3\text{PbI}_3$  PhC bandedge laser device: (c) top surface of the perovskite film and (d) cross-section of the device, shown sequentially from  $\text{SiO}_2$  to  $\text{CH}_3\text{NH}_3\text{PbI}_3$  thin film. The dotted lines in (b) and (d) are for eye-guide.

### 3.2.3 Photonic band structure of perovskite PhC bandedge laser

Figure 3-2-4(a) shows photonic band structure of a model square lattice 2D PhC slab structure, which is calculated using plane wave expansion (PWE) method. Also, Figs. 3-2-4(b) and (c) are magnified band structure of each bandedge modes,  $\Gamma$ - and M-point, respectively. The refractive indices of the perovskite  $\text{CH}_3\text{NH}_3\text{PbI}_3$  film was obtained from spectroscopic ellipsometer measurements on an independently but identically prepared homogeneous perovskite film where  $n$  is 2.56 at the center emission wavelength of  $\lambda = 780$  nm. From the band structure, we find distinct bandedge modes at  $\Gamma$ - and M-points, which can be used for bandedge lasing action. In order to explore the two possibilities, we prepared two kinds of PhC patterns with different lattice constants and air-hole diameters; ( $a_\Gamma = 345$  nm;  $\varphi_\Gamma = 150$  nm for  $\Gamma$ -point bandedge laser) and ( $a_M = 255$  nm;  $\varphi_M = 100$  nm for M-point bandedge laser). The lattice constants  $a_\Gamma$  and  $a_M$  are chosen such that the emission band of the active material,  $\text{CH}_3\text{NH}_3\text{PbI}_3$  perovskite thin film, coincides with the photonic bandedges at  $\Gamma$ - and M-points, respectively. Therefore, we expect lasing actions at the  $\Gamma$ - and M-point bandedge modes from the two samples; for this reason, we will call the two types of samples  $\Gamma$  and M, respectively. Note that the energy levels of some bandedge modes are degenerate such as  $\Gamma_1 \leftrightarrow \Gamma_2$  and  $M_0 \leftrightarrow M_1$ . Figures 3-2-5(a) and (b) are modal spectra calculated for samples  $\Gamma$  and M with by finite-difference time-domain (FDTD) simulations (FDTD Solutions, Lumerical Solutions, Inc.). Well-defined bandedge modes are clearly supported by the structures. Shown as the insets in Figs. 3-2-5(a) and (b) are the transverse electric field intensity profiles for the  $\Gamma$ - and M-point bandedge modes which are the strongest bandedge modes overlapped with the emission band of perovskite material.

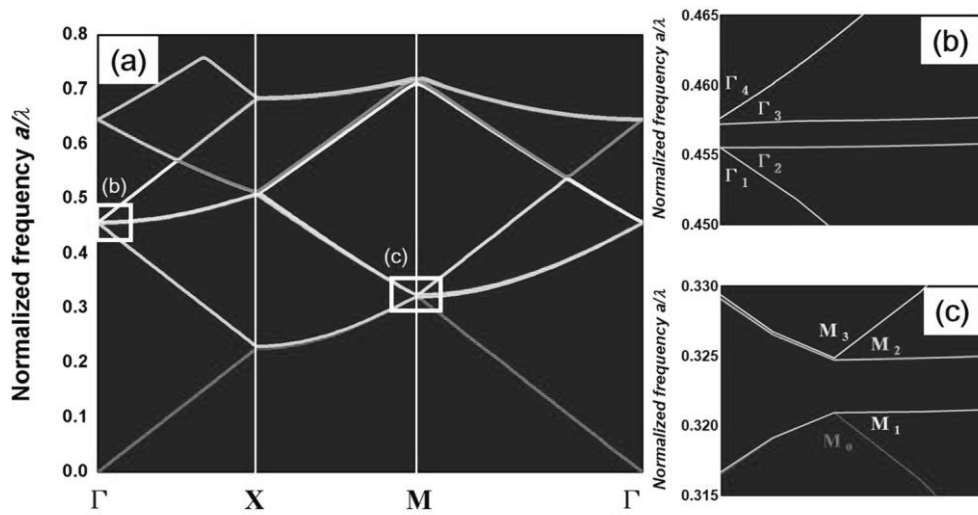


Figure 3-2-4 (a) Photonic band structure of the  $\text{CH}_3\text{NH}_3\text{PbI}_3$  PhC bandedge laser structure, calculated by the plane-wave expansion method. Also shown in the right are magnified band structures near (b)  $\Gamma$ - and (c)  $M$ -points, which are marked by square boxes in (a).

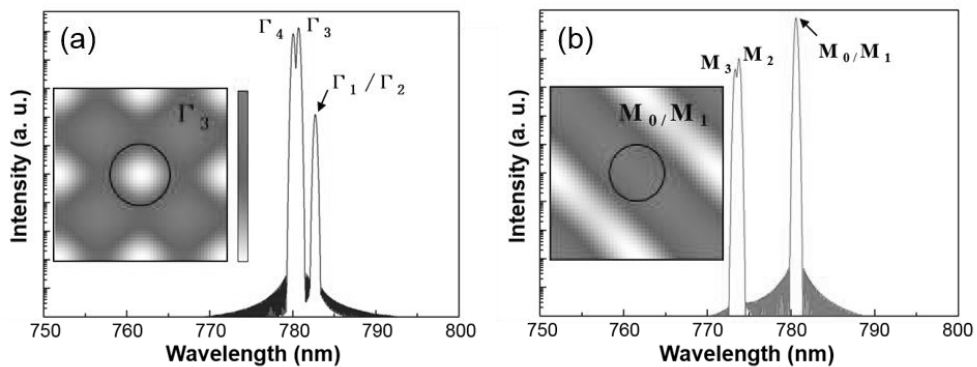


Figure 3-2-5 Mode spectra for (a) sample  $\Gamma$  and (b) sample  $M$ , both simulated by FDTD method. For each case, the inset shows the modal pattern calculated for the strongest bandedge mode.

### 3.3 Results and discussion

#### 3.3.1 Measurement with polarization dependence

Fabricated devices were optically pumped using a 532 nm frequency-doubled Nd:YAG laser in pulsed mode (pulse width 400 ps; repetition rate 1 kHz). A 20× objective lens (NA = 0.4) was used to focus pump laser beam to a spot of ~70 μm in diameter. Figure 3-3-1 is a schematic diagram of lens based micro-photoluminescence (PL) setup.

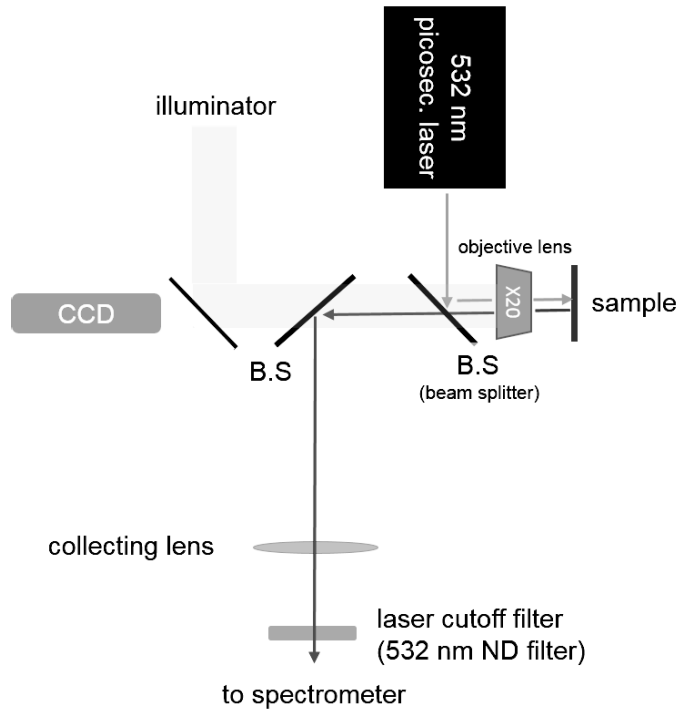


Figure 3-3-1 Schematic diagram of lens based micro-PL setup.

The emission spectra from the two samples  $\Gamma$  and M, taken at various excitation levels, are shown in Figs. 3-3-2(a) and (b). Both samples exhibit laser threshold, above which sharp stimulated emission peaks appear newly on the broad background

spontaneous emission. As we expected, the emission spectra clearly indicate that the both lasers operate in single mode which is from the nature of bandedge modes. The light input versus output relationships are plotted in the insets for both modes. The abrupt changes in slope are clear indication of the onset of lasing action. Pulse energy densities at laser threshold are similar for the both samples,  $\sim 200 \mu\text{J}/\text{cm}^2$ . We also examined polarization dependence of laser emission, and the measured results are summarized in Figs. 3-3-2(c) and (d). As we expected, sample  $\Gamma$  exhibits an isotropic polarization dependence, consistent with the electric field profile shown in Fig. 3-2-5(a). This isotropic polarization dependence is compatible with the notion that there is no preferred direction for the electric field as the momentum vector of the  $\Gamma$ -point is in the vertical direction (or parallel to the direction of detection). In good contrast, sample M has two main lobes stretched along the directions toward M-points, which is compatible with the modal pattern shown in Fig. 3-2-5(b). This anisotropic polarization dependence with the long axis aligns along the M-points. It should be fair to say that although the M-point bandedge is an in-plane mode, it can still be detected in the vertical direction via coherent scatterings (thus its polarization information being preserved partially).

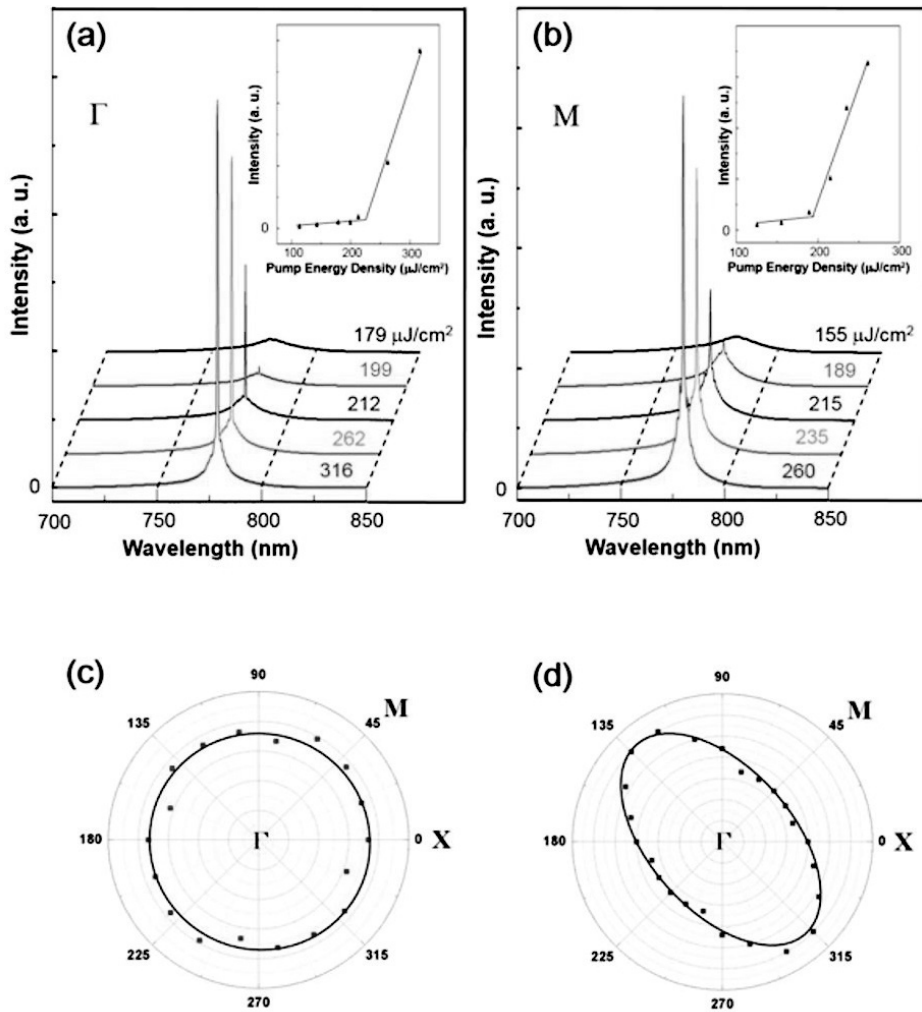


Figure 3-3-2 Emission spectra from the  $\text{CH}_3\text{NH}_3\text{PbI}_3$  PhC bandedge lasers recorded at various excitation levels: (a) sample  $\Gamma$  and (b) sample M. Each inset presents the relationship between light input and output. Measured polarization dependence of light output: (c) sample  $\Gamma$  and (d) sample M. The directions of the reciprocal lattice vectors ( $\Gamma$ , X, and M) are marked.

### 3.4 Summary

We demonstrated room temperature single mode lasing from the hybrid perovskite  $\text{CH}_3\text{NH}_3\text{PbI}_3$  successfully. A single lasing mode was originally defined by a bandedge mode of 2D square lattice PhC backbone structure, while optical gain necessary for laser action was provided by a thin hybrid perovskite film spin-coated on top of the PhC backbone. Two kinds of devices for  $\Gamma$ - and M-points were designed and fabricated to operate with different bandedge modes. When pumped optically, both devices lased in single mode with the polarization properties expected from the bandedge modes. This work proves that the hybrid perovskite material is now mature enough to be used not only for photovoltaics application but also for highly functional light-emitting devices. In addition, we believe that it also brightens *hybrid photonics*, in which passive photonic structures are hybridized extrinsically with active optical materials to build sophisticated photonic integrated circuits for near future.

## References

- [1] S. D. Stranks, G. E. Eperon, G. Grancini, C. Menelaou, M. J. P. Alcocer, T. Leijtens, L. M. Herz, A. Petrozza, and H. J. Snaith, “Electron-hole diffusion lengths exceeding 1 micrometer in an organometal trihalide perovskite absorber,” *Science*, **342**, 341-344, (2013).
- [2] G. Xing, N. Mathews, S. Sun, S. S. Lim, Y. M. Lam, M. Grätzel, S. Mhaisalkar, and T. C. Sum, “Long-range balanced electron and hole-transport lengths in organic-inorganic  $\text{CH}_3\text{NH}_3\text{PbI}_3$ ,” *Science*, **342**, 344-347, (2013).
- [3] C. Wehrenfennig, G. E. Eperon, M. B. Johnston, H. J. Snaith, and L. M. Herz, “High charge carrier mobilities and lifetimes in organolead trihalide perovskites,” *Advanced Materials*, **26**, 1584-1589, (2014).
- [4] F. Deschler, M. Price, S. Pathak, L. E. Klintberg, D.-D. Jarausch, R. Higler, S. Hüttner, T. Leijtens, S. D. Stranks, H. J. Snaith, M. Atatüre, R. T. Phillips, and R. H. Friend, “High photoluminescence efficiency and optically pumped lasing in solution-processed mixed halide perovskite semiconductors,” *Journal of Physical Chemistry Letters*, **5**, 1421-1426, (2014).
- [5] Z.-K. Tan, R. S. Moghaddam, M. L. Lai, P. Docampo, R. Higler, F. Deschler, M. Price, A. Sadhanala, L. M. Pazos, D. Credgington, F. Hanusch, T. Bein., H. J. Snaith and R. H. Friend, “Bright light-emitting diodes based on organometal halide perovskite,” *Nature Nanotechnology*, **9**, 687-692, (2014).
- [6] G. Xing, N. Mathews, S. S. Lim, N. Yantara, X. Liu, D. Sabba, M. Grätzel, S. Mhaisalkar, and T. C. Sum, “Low-temperature solution-processed wavelength-tunable perovskites for lasing,” *Nature Materials*, **13**, 476-480, (2014).
- [7] A. Kojima, K. Teshima, Y. Shirai, and T. Miyasaka, “Organometal halide

- perovskites as visible-light sensitizers for photovoltaic cells,” *Journal of the American Chemical Society*, **131**, 6050-6051, (2009).
- [8] W. S. Yang, J. H. Noh, N. J. Jeon, Y. C. Kim, S. Ryu, J. Seo, and S. I. Seok, “High-performance photovoltaic perovskite layers fabricated through intramolecular exchange,” *Science*, **348**, 1234-1237, (2015).
- [9] M. M. Lee, J. Teuscher, T. Miyasaka, T. N. Murakami, and H. J. Snaith, “Efficient hybrid solar cells based on meso-superstructured organometal halide perovskites,” *Science*, **338**, 643-647, (2012).
- [10] H. Zhou, Q. Chen, G. Li, S. Luo, T.-B. Song, H.-S. Duan, Z. Hong, J. You, Y. Liu, and Y. Yang, “Interface engineering of highly efficient perovskite solar cells,” *Science*, **345**, 542-546, (2014).
- [11] N.-G. Park, “Organometal perovskite light absorbers toward a 20% efficiency low-cost solid-state mesoscopic solar cell,” *Journal of Physical Chemistry Letters*, **4**, 2423-2429, (2013).
- [12] H. Zhu, Y. Fu, F. Meng, X. Wu, Z. Gong, Q. Ding, M. V. Gustafsson, M. T. Trinh, S. Jin, and X.-Y. Zhu, “Lead halide perovskite nanowire lasers with low lasing thresholds and high quality factors,” *Nature Materials*, **14**, 636-643, (2015).
- [13] Q. Liao, K. Hu, H. Zhang, X. Wang, J. Yao, and H. Fu, “Perovskite microdisk microlasers self-assembled from solution,” *Advanced Materials*, **27**, 3405-3410, (2015).
- [14] Q. Zhang, S. T. Ha, X. Liu, T. C. Sum, and Q. Xiong, “Room-temperature near-infrared high-Q perovskite whispering-gallery planar nanolasers,” *Nano Letters*, **14**, 5995-6001, (2014).

- [15] R. Dhankar, A. N. Brigeman, A. V. Larsen, R. J. Stewart, J. B. Asbury, and N. C. Giebink, "Random lasing in organo-lead halide perovskite microcrystal networks," *Applied Physics Letters*, **105**, 151112, (2014).
- [16] S. Kim, S. Ahn, K. Min, S. Kim, H. Jeon, P. Regreny, and C. Seassal, "Nano stepping-stone laser," *Applied Physics Express*, **6**, 042703, (2013).
- [17] D.-U. Kim, S. Kim, J. Lee, S.-R. Jeon, and H. Jeon, "Free-standing GaN-based photonic crystal band-edge laser," *IEEE Photonics Technology Letters*, **23**, 1454-1456, (2011).
- [18] V. Reboud, P. Lovera, N. Kehagias, M. Zelsmann, C. Schuster, F. Reuther, G. Gruetzner, G. Redmond, and C. M. Sotomayor Torres, "Two-dimensional polymer photonic crystal band-edge lasers fabricated by nanoimprint lithography," *Applied Physics Letters*, **91**, 151101, (2007).
- [19] S. Kim, S. Ahn, J. Lee, H. Jeon, P. Regreny, C. Seassal, E. Augendre, and L. Di Cioccio, "Milliwatt-level fiber-coupled laser power from photonic crystal band-edge laser," *Optics Express*, **19**, 135101, (2011).
- [20] S. Kim, S. Kim, K. Hwang, H. Jeon, and H. J. Kim, "Operation of photonic crystal laser in continuous-wave mode for 18 hours," *Applied Physics Express*, **4**, 122101, (2011).
- [21] M. Jiang, J. Wu, F. Lan, Q. Tao, D. Gao, and G. Li, "Enhancing the performance of planar organo-leadhalide perovskite solar cells by using a mixed halide source," *Journal of Materials Chemistry A*, **3**, 963-967, (2015).
- [22] M. Liu, M. B. Johnston, and H. J. Snaith, "Efficient planar heterojunction perovskite solar cells by vapour deposition," *Nature*, **501**, 395-398,22 (2013).

## Chapter 4

# Visible wavelength distributed feedback laser from formamidinium lead halide perovskite thin films with TE/TM mode selection

### 4.1 Introduction

During the past few years, organic-inorganic lead halide perovskite has been demonstrated to be an alternative light harvester with great power conversion efficiency (PCE) in photovoltaics research area. To date, the highest power conversion efficiency of perovskite cells has been reported as 22.1% [1]. A number of unique properties of lead halide perovskite such as a large absorption coefficient in visible range regime [2], long diffusion length and carrier lifetime [3,4], and high photoluminescence (PL) quantum efficiency [5] has attracted significant attention as a good light emitter for optoelectronic application. Also, by controlling the halide composition between bromide and iodide in the material, the wavelength can be easily tuned from 500 nm to 800 nm which is in visible range [6]. This stoichiometric wavelength tunability is a huge benefit to make this material as promising candidates for the variety of optoelectronic applications, such as light-emitting diode [7], laser [8], and sensor [9]. Based on these advantages of hybrid perovskite, there are various optical resonator lasers have been already demonstrated, including the nanowire [10], microdisk [11], distributed Bragg reflector (DBR) [12], and random networks [13]. However, there is one major obstacle exists for applying those to the optical

communication and computing system because of the multi-mode laser operation. Usually, the single mode operation is a crucially important property for sophisticated and complex photonic integrated circuit. Additionally, the ultimate goals of this kind of lasers is to operate with continuous-wave (CW) lasing or electrically driven lasing. However, most recently studied light-absorbing material is methylammonium lead triiodide (MAPbI<sub>3</sub>), which shows reversible phase transition at 55 °C and instability under illumination and elevated temperature condition due to low crystallization energy was reported as weak points of MAPbI<sub>3</sub> [14-17]. To overcome the disadvantages of MAPbI<sub>3</sub>, alternatives of methylammonium cation are investigated and formamidinium (FA) cation was suggested. Compared to MAPbI<sub>3</sub>, formamidinium lead triiodide (FAPbI<sub>3</sub>) absorbs wider range of light due to its reduced band gap energy and shows longer charge diffusion length and superior stability against the light and heat [18-21]. Furthermore, band gap is easily tuned by incorporation of bromide which also improved the stability of photovoltaic cells [22]. In this study, we choose FA instead of MA which is used in our previous study and tune the band gap of perovskite by incorporation of bromide to examine the laser behavior in visible light region. Also, for supporting the single mode lasing, we adopt a one-dimensional (1D) distributed feedback structure as backbone to combine this passive structure with FA-based perovskite, CH(NH<sub>2</sub>)<sub>2</sub>Pb(Br<sub>0.6</sub>I<sub>0.4</sub>)<sub>3</sub>, thin film as active optical medium through simple spin-casting method. This 1D distributed feedback (DFB) structure was generated by laser interference lithography (LIL) technique with the advantages of submicron scale pattern on large area, high throughput, and cost effectiveness [23]. In addition, by optimizing the simple spin-casting method, we achieved the high quality CH(NH<sub>2</sub>)<sub>2</sub>Pb(Br<sub>0.6</sub>I<sub>0.4</sub>)<sub>3</sub> closely packed thin film with uniform and conformal surface morphology. In this research, we demonstrate optically pumped single mode lasing from hybrid perovskite CH(NH<sub>2</sub>)<sub>2</sub>Pb(Br<sub>0.6</sub>I<sub>0.4</sub>)<sub>3</sub> thin film fabricated on the 1D DFB structure, and show the possibility of mode selections for both transverse electric (TE) and transverse magnetic (TM) mode by slightly changing the structural parameters.

## 4.2 1D DFB laser with perovskite $\text{FAPb}(\text{Br}_{0.6}\text{I}_{0.4})_3$

### 4.2.1 Preparation of $\text{CH}(\text{NH}_2)_2\text{Pb}(\text{Br}_{0.6}\text{I}_{0.4})_3$ perovskite material

Processing solution is prepared by simple mixing of  $\text{FAPbI}_3$  and  $\text{FAPbBr}_3$  precursor solutions in certain ratio. Target band gap is  $\sim 2$  eV with optical absorption edge at  $\sim 600$  nm. When 4:6 v/v mixture ( $\text{FAPbI}_3$  solution: $\text{FAPbBr}_3$  solution) is used as processing solution,  $\text{FAPb}(\text{Br}_{0.6}\text{I}_{0.4})_3$  film with band gap of  $\sim 2$  eV is successfully fabricated as shown in Fig. 4-2-1. The atomic concentration of iodide and bromide is identified by X-ray photoelectron spectroscopy and was estimated to be 12.73:9.02 by comparing characteristic of Br  $3d$  and I  $3d_5$  which is in a good agreement with feed ratio.  $\text{FAPb}(\text{Br}_{0.6}\text{I}_{0.4})_3$  film morphology are characterized by scanning electron microscopy (SEM) and atomic force microscopy (AFM). As shown in Fig. 4-2-2, the film exhibits very smooth surface with 100 ~ 200 nm-sized crystallites and 15.9 nm of root-mean-square (RMS) roughness was calculated by AFM image as the insets in Fig. 4-2-2.  $\text{FAPb}(\text{Br}_{0.6}\text{I}_{0.4})_3$  morphology are optimized by solvent engineering method with Lewis base adduct concept and the film morphology is great improvement compared to  $\text{MAPbI}_3$  film morphology in our previous work [24,25].

When bromide ion is incorporated to  $\text{FAPbI}_3$  (or  $\text{MAPbI}_3$ ) crystal, crystal structure is gradually changed from  $\text{FAPbI}_3$  (or  $\text{MAPbI}_3$ ) crystal to  $\text{FAPbBr}_3$  (or  $\text{MAPbBr}_3$ ) as bromide content is increased [20,22]. According to single crystal X-ray diffraction (XRD) in the reported literature of Zhumeckenov et. al.,  $\text{FAPbI}_3$  and  $\text{FAPbBr}_3$  have same cubic crystal structure (space group: Pm-3m) with lattice parameters of  $a = 6.3573 \text{ \AA}$  and  $a = 5.9944 \text{ \AA}$ , respectively. Space group (Pm-3m) and lattice parameter of  $\text{FAPb}(\text{Br}_{0.6}\text{I}_{0.4})_3$  film is deduced by XRD pattern which is shown in Fig. 4-2-3 and  $\text{FAPb}(\text{Br}_{0.6}\text{I}_{0.4})_3$  crystal has same space group, Pm-3m as

FAPbI<sub>3</sub> and FAPbBr<sub>3</sub> crystals with lattice parameter lattice parameter,  $a = 6.0482 \text{ \AA}$  which is positioned between lattice parameters of FAPbI<sub>3</sub> and FAPbBr<sub>3</sub>. In Fig. 4-2-2, perovskite film morphology was characterized using scanning electron microscopy (SEM, Inspect F, FEI) and atomic force microscopy (AFM, XE-100, Park Systems). In Fig. 4-2-3, Crystal information of FAPb(Br<sub>0.6</sub>I<sub>0.4</sub>)<sub>3</sub> perovskite was identified by XRD pattern obtained from X-ray diffractometer (DMAX 2500, Rigaku) using Cu-K $\alpha$  radiation ( $\lambda = 1.5418 \text{ \AA}$ ) at a scan rate of  $2^\circ \text{ min}^{-1}$ .

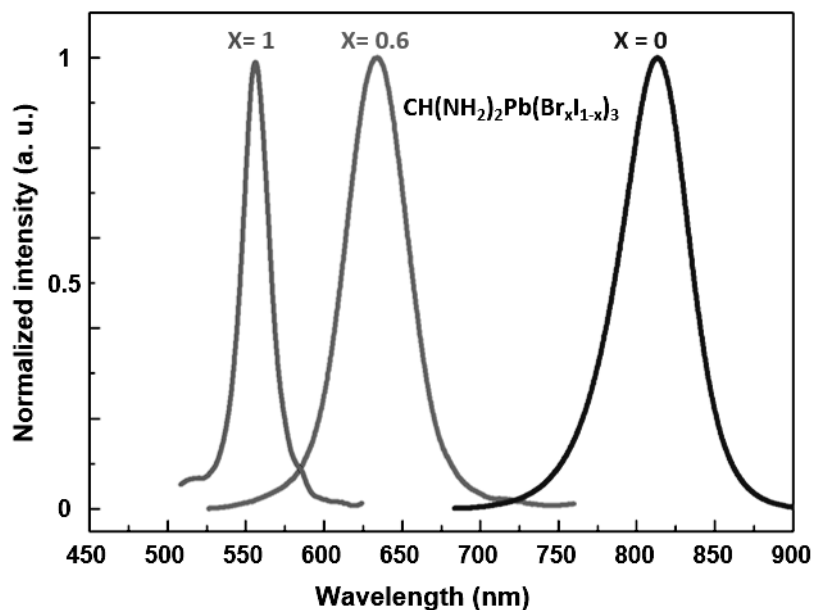


Figure 4-2-1 Photoluminescence of different FA-based perovskite thin film from 500 nm to 900 nm.

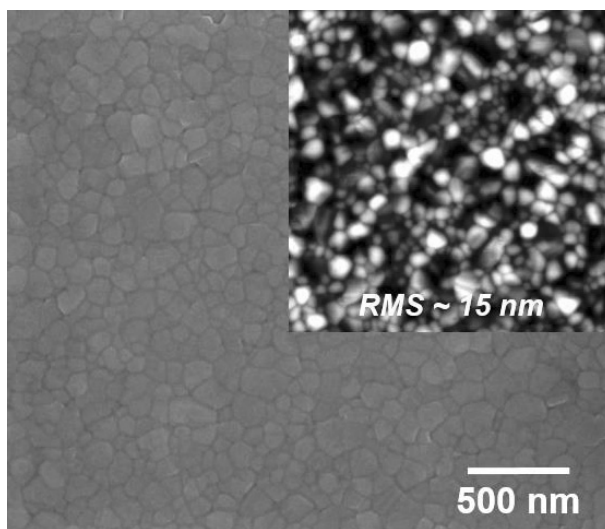


Figure 4-2-2 Scanning electron microscopy and atomic force microscopy of  $\text{FAPb}(\text{Br}_{0.6}\text{I}_{0.4})_3$  film.

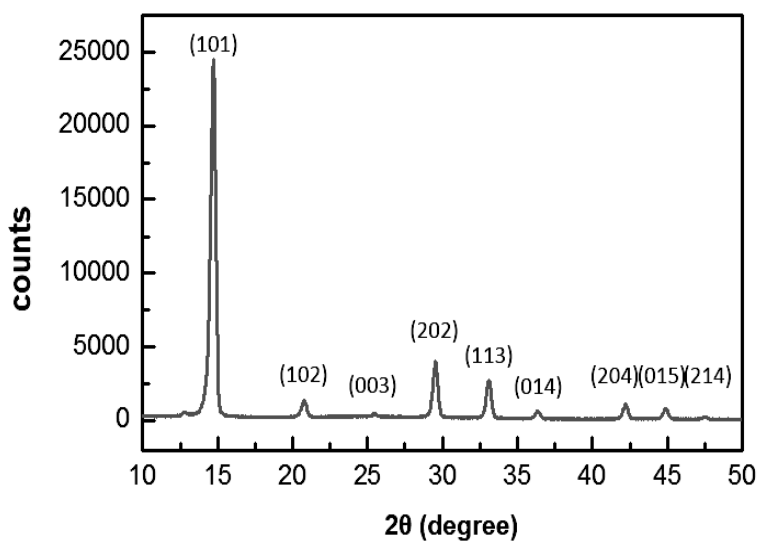


Figure 4-2-3 Crystal information of  $\text{FAPb}(\text{Br}_{0.6}\text{I}_{0.4})_3$  perovskite thin film from X-ray diffractometer.

## 4.2.2 Device fabrication

Overall device structure of  $\text{CH}(\text{NH}_2)_2\text{Pb}(\text{Br}_{0.6}\text{I}_{0.4})_3$  DFB laser is schematically drawn in Fig. 4-2-4(a). There are two independent and parallel preparations needed for the device; one is FA-based perovskite thin film, and the other is 1D DFB structure as backbone. The preparation of  $\text{CH}(\text{NH}_2)_2\text{Pb}(\text{Br}_{0.6}\text{I}_{0.4})_3$  perovskite thin film is as follows: Formamidinium iodide (FAI) and formamidinium bromide (FABr) are purchased from Dyesol and lead (II) iodide ( $\text{PbI}_2$ ) and lead (II) bromide ( $\text{PbBr}_2$ ) are purchased from Alfa Aesar and Sigma-Aldrich, respectively. Processing solution for  $\text{FAPb}(\text{Br}_{0.6}\text{I}_{0.4})_3$  are made by mixing 0.6 mL of  $\text{FAPbBr}_3$  precursor solution and 0.4 mL of  $\text{FAPbI}_3$  precursor solution. To make  $\text{FAPbBr}_3$  and  $\text{FAPbI}_3$  precursor solution, 1 mmol of organic compound (FABr for  $\text{FAPbBr}_3$  precursor solution and FAI for  $\text{FAPbI}_3$  precursor solution) and 1 mmol of inorganic compound ( $\text{PbBr}_2$  for  $\text{FAPbBr}_3$  precursor solution and  $\text{PbI}_2$  for  $\text{FAPbI}_3$  precursor solution) are mixed in a 10 mL vial and 1.2 mL of *N, N*-dimethylformamide (DMF) and 0.071 mL of dimethyl sulfoxide (DMSO) are added to the mixture. Two solutions are stirred for more than 3 hours to dissolve organic and inorganic compound completely and are used within a day. Quartz substrate was cleaned by stepwise sonication in detergent solution, water, acetone and isopropanol for 15 mins each then was dried at 80 °C. After complete drying, the substrate was treated with UV-ozone for 20 mins and transferred to a  $\text{N}_2$ -filled glove box.  $\text{FAPb}(\text{Br}_{0.6}\text{I}_{0.4})_3$  precursor solution was spin-coated on the substrate at 1000 rpm for 5 sec then at 4000 rpm for 15 sec. Diethyl ether was dropped on the substrate during the spin-coating on second stage. The substrate was moved to hot plate (110 °C) immediately and annealed for 10 mins.

The next sample preparation procedure for DFB part is as follows: The prepared quartz substrate 1cm x 1cm in size was washed by acetone, isopropanol (IPA), and

deionized water cleaning process, then a 50-nm-thick Cr layer as hard mask was deposited on the base substrate by metal evaporation. After that, a fine-resolution photoresist (AZ MiR 701, Microchemicals GmbH) was spin-coated on the substrate with 4000 rpm to obtain a 250 nm thick photoresist layer. After 1 min soft-baking, the sample was mounted on the laser interference lithography (LIL) rotational stage to make a 1D DFB pattern on the sample. In our LIL setup, a 266 nm diode-pumped solid-state (DPSS) laser beam is expanded through the spatial filter, and it reaches to the exposure stage shown in Fig. 4-2-6 [26]. By controlling the angle between the reflected beam from mirror and incident beam, the interference beam which is directly incident on the photoresist decides the grating pitch of 1D DFB pattern. Also, the filling factor of the 1D DFB pattern is controlled by the exposure time and development time. Finally, subsequent pattern transfer to the base substrate was accomplished by a selective reactive-ion etch (RIE); for this purpose, we selected RIE gas mixture of  $\text{Cl}_2$  and  $\text{O}_2$  for Cr hard mask and standard RIE gas mixture of  $\text{CF}_4$  and  $\text{O}_2$  for quartz substrate, respectively. Figure 4-2-4(b) shows the scanning electron microscopy (SEM) images from the fabricated 1D grating pattern on quartz substrate. We were able to confirm that 1D grating pattern is well defined over the entire substrate, and we could see another evidence simply by eyes with the photographic image of Fig. 4-2-5(c) which shows homogeneous diffraction color through the entire sample. Figure 4-2-5(a) is a cross sectional SEM image of local area of the sample after hybrid perovskite  $\text{CH}(\text{NH}_2)_2\text{Pb}(\text{Br}_{0.6}\text{I}_{0.4})_3$  thin film is spin coated over 1D grating pattern on the quartz substrate. From this, we can recognize the hybrid perovskite thin film consists of highly close packing of crystalline grains with having less pinholes which are well-known problem when using the spin-casting method like one-step deposition process. From Fig. 4-2-5(b), we also know the hybrid perovskite thin film

uniformly coated through entire sample by looking the clear optical transparency of the film.

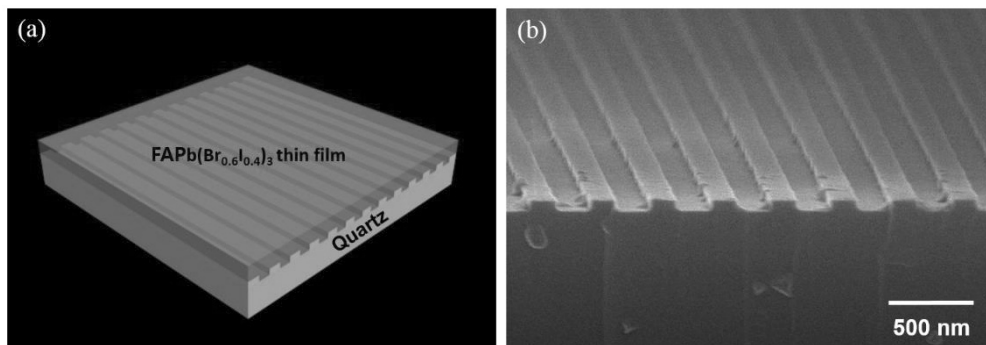


Figure 4-2-4 (a) Schematic of the  $\text{CH}(\text{NH}_2)_2\text{Pb}(\text{Br}_{0.6}\text{I}_{0.4})_3$  1D DFB laser structure. (b) Scanning electron microscopy (SEM) images from the fabricated 1D grating pattern on quartz substrate

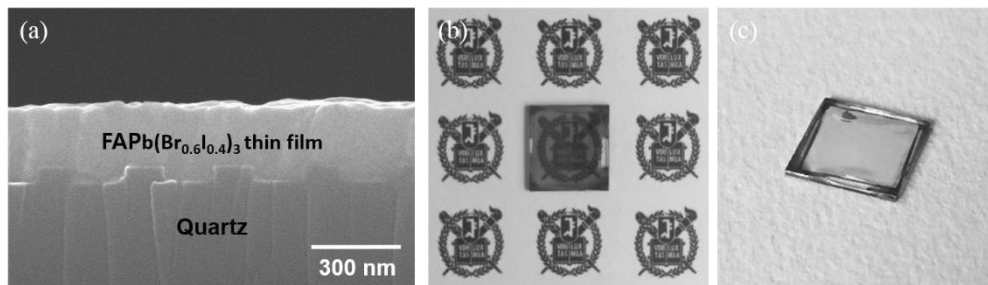


Figure 4-2-5 (a) Cross sectional SEM image of local area of the sample after hybrid perovskite  $\text{CH}(\text{NH}_2)_2\text{Pb}(\text{Br}_{0.6}\text{I}_{0.4})_3$  thin film (b) demonstrating optical transparency of the thin film (c) photographic image of 1D grating pattern.

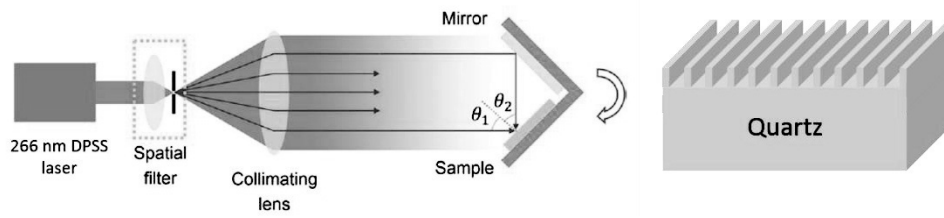


Figure 4-2-6 Schematic of the LIL setup based on a Lloyd's mirror interferometer and fabricated 1D grating on quartz substrate [26].

### 4.2.3 TE/TM mode selection

The polarization handling is a key feature for almost every photonic system from optical communication to bio-sensing. Especially, in the photonic integrated circuits and their applications, this manipulation is the one of the main concern because the waveguides is strongly polarization dependent, and as a pumping beam source, it also related to the pumping efficiency for overall device. Therefore, we have a structural design configuration which can select TE/TM polarization of direction of light simply by the change of the parameters in the structure. Figures 4-2-7 and 4-2-8 show the modal spectrum and profile for both differently polarized DFB lasers such as TE and TM, which are calculated using finite-difference time-domain (FDTD) simulation from FDTD solution, Lumerical Solution, Inc. Based on the information of refractive indices from the spectroscopic ellipsometer measurement, we use the refractive index of hybrid thin film as  $\sim 2.14$  for the emission peak wavelength of  $\lambda = 640$  nm, and we design the second order DFB grating structure for the device because this geometry supports the vertical direction of emission of light which is perpendicular to the grating surface while the optical feedback is in-plane direction. With 2<sup>nd</sup> order DFB grating structure, the grating period is almost twice longer than 1<sup>st</sup> order DFB one for lasing, so it makes the fabrication process much easier. Also, due to the vertical direction of emission of light, it is suitable for the fiber coupling and the alignment for measurement. According to the simulations, we prepared two kinds of DFB structure by changing the grating periods ( $\Lambda$ ) with fixed film thicknesses (T): ( $\Lambda_{TE} = 330$  nm;  $T_{TE} = 240$  nm) and ( $\Lambda_{TM} = 345$  nm;  $T_{TE} = 240$  nm). Due to the difference between DFB structure backbone and hybrid perovskite thin film of refractive index, we were able to secure the sufficient mode separation in spectrum range, so we could select the only one mode (either TE or TM) can survive in the emission band of the

optical gain,  $\text{CH}(\text{NH}_2)_2\text{Pb}(\text{Br}_{0.6}\text{I}_{0.4})_3$  thin film by simply changing the parameters in the structure. Figures 4-2-7 shows details of TE and TM modal spectrum, respectively: where the blue color represents TE mode resonance and red as TM resonance. The shaded area is the emission band of optical gain material with full width at half maximum (FWHM),  $\sim 30$  nm. As we expected, there is only one resonance peak stays in the emission band of optical gain with our designed structural parameters. Therefore, we expect the lasing actions from two differently polarized DFB laser. From Figs. 4-2-8(a) and (b), we can also confirm well-defined TE/TM fundamental modes are identified by the structure. The reason why we chose the fundamental mode is simple because of maximizing the mode overlap with gain material without nodes.

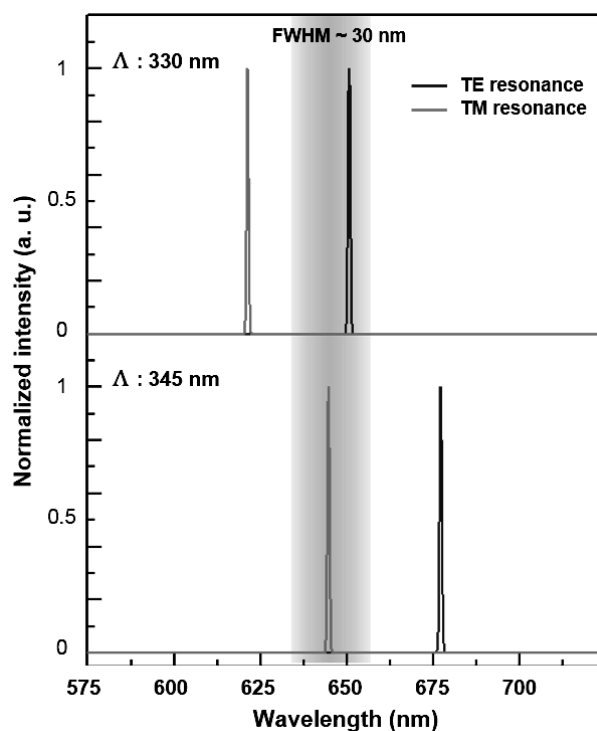


Figure 4-2-7 Mode spectra for (a) TE mode and (b) TM mode, by FDTD simulation.

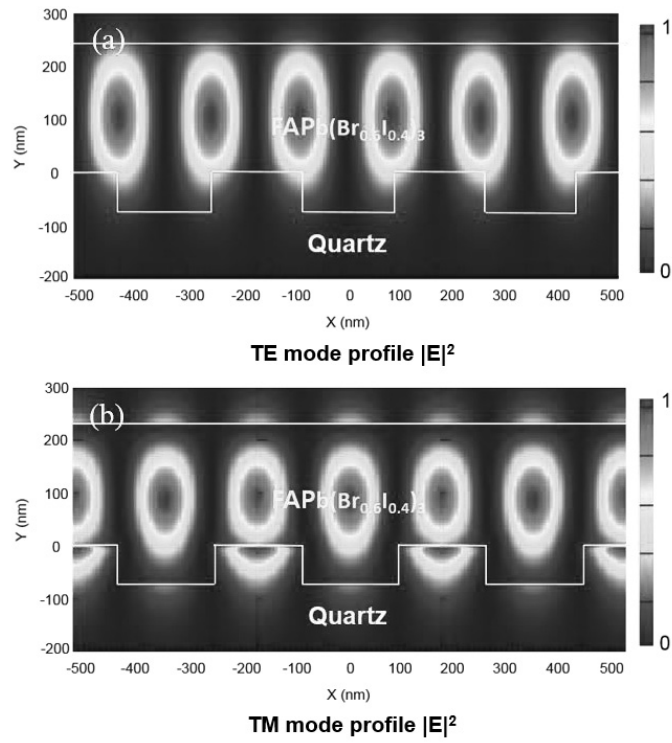


Figure 4-2-8 Mode profiles for (a) TE mode and (b) TM mode. These are well-defined TE/TM fundamental modes by the structure.

## 4.3 Results and discussion

### 4.3.1 Measurement with polarization dependence

Fabricated device was optically pumped using a frequency-doubled 532 nm Nd:YAG laser in a pulsed mode (pulse width 400 ps; repetition rate 1 kHz). The size of the beam passing through the pinhole was fixed and controlled the beam waist by plano-convex cylindrical lens. So, the focused pump laser beam size on the grating surface was 2 mm x 0.2 mm. The emitted light was detected using a spectrometer (Dongwoo Corp., DM700) along the normal to the grating surface. We also have examined lasing characteristics after cooled down to the cryogenic temperature, 77 K with liquid nitrogen. Figure 4-3-1 is a schematic diagram of cylindrical lens based PL setup

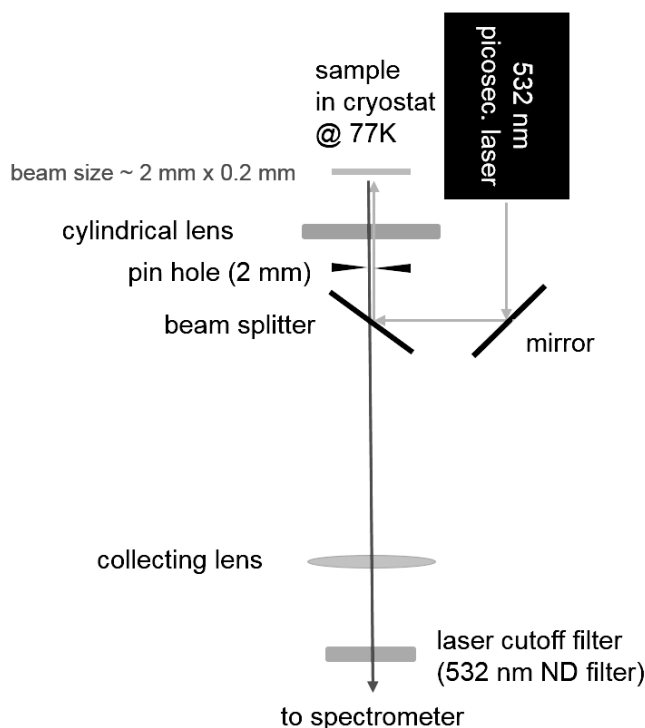


Figure 4-3-1 Schematic diagram of cylindrical lens based PL setup.

Shown in Figs. 4-3-2(a) and (b) are emission spectra from two different samples, TE and TM mode, taken under different pump fluence. As we expected, both emission spectra with different pumping level show clear single mode laser characteristics with narrow linewidth. In each spectrum, there is a little bump, which is located right next to the single peak, is amplified spontaneous emission (ASE) peak from planar thin film of  $\text{CH}(\text{NH}_2)_2\text{Pb}(\text{Br}_{0.6}\text{I}_{0.4})_3$ . From the measurement, we realized the results are in a good agreement with our FDTD simulation spectra data. We also plotted light input vs. output curves as the insets. Both samples clearly show the threshold region known as a “kink” which is between the two linear regions of spontaneous emission and stimulated emission. This “kink” is a strong indication of starting point of lasing action. Pulse energy densities at laser threshold level are  $\sim 20 \text{ mJ/cm}^2$  and  $\sim 3 \text{ mJ/cm}^2$  for TE and TM mode, respectively. The threshold level for TE mode is higher than TM mode. With these single mode lasing characteristics, we also wanted to verify one more lasing characteristic which is a polarization. For that, we put a linear circular polarizer in front of the spectrometer and examined polarization dependence for both lasers, and the results show in Figs. 4-3-2(c) and (d). Both samples exhibit highly polarized characteristics in one direction, either parallel to the grating line or perpendicular to the grating line. In the case of TE mode, we consider the electric field oscillation is parallel to the direction of grating line, and we verify this preferred direction compared to the measured polarization direction. In the case of TM mode, the measured polarization is 90 degree rotated compared to the polarization of TE mode. This result coincides with our expectation because electric field oscillations for TM mode coexist in the direction of perpendicular to the grating line and normal to the grating plane. However, electric field oscillation from the normal component is hard to recognize by polarizer due to the direction. Therefore, only one direction which is perpendicular to the grating line is clearly revealed by the polarizer, and we could confirm that from Fig. 4-3-2(d).

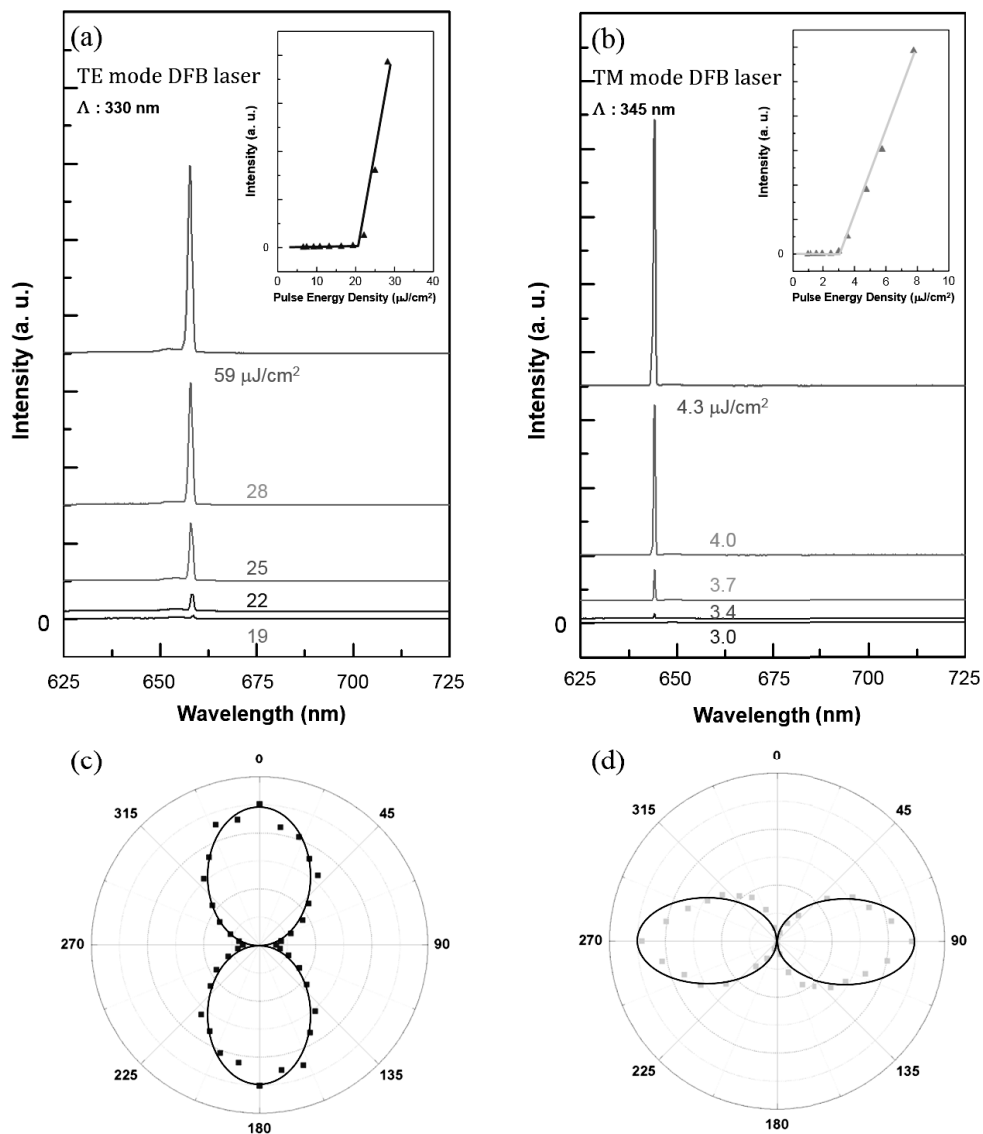


Figure 4-3-2 Emission spectra from the  $\text{CH}(\text{NH}_2)_2\text{Pb}(\text{Br}_{0.6}\text{I}_{0.4})_3$  1D DFB laser at various excitation levels: (a) TE and (b) TM mode. Each inset shows the relationship between light input and output. Measured polarization dependence of light output: (c) TE and (d) TM mode.

### 4.3.2 Temperature dependence for $\text{FAPb}(\text{Br}_{0.6}\text{I}_{0.4})_3$ 1D DFB laser and PL

As previously explained, we did our overall optical pumping measurement at cryogenic temperature, 77 K because there is only ASE shown under room temperature condition, not shown any DFB TE/TM modes. So, we decreased the temperature from 300 K to 77 K gradually to see what happens in the sample, typically for lasing action. When the temperature reached at 200 K, then suddenly the mode appeared and it lased while increasing the pump fluence. We did this temperature dependent experiment about DFB TM mode laser. The results of light input versus output relationship at selected temperatures are summarized in Fig 4-3-3. As the temperature decreased, thresholds were reduced to  $\sim 3 \text{ mJ/cm}^2$  and slope efficiency was increased. These two parameters tell us that the laser performance is better under low temperature because of controlling the heat dissipation by cooling to liquid nitrogen temperature. Except the heat dissipation, we tried to find the other factors to prevent becoming a lasing action. One thing we suspected is due to a change in the material itself while the temperature cooled down. So, we examined temperature dependent of thin film of  $\text{CH}(\text{NH}_2)_2\text{Pb}(\text{Br}_{0.6}\text{I}_{0.4})_3$  deposited on the bare quartz substrate. Figure 4-3-4 shows the temperature-dependent spectra of  $\text{CH}(\text{NH}_2)_2\text{Pb}(\text{Br}_{0.6}\text{I}_{0.4})_3$  thin film. As temperature decreased from 300 K to 77 K, only one emission peak was observed with monotonous peak red-shifting, and linewidth of PL was narrowed down to  $\sim 30 \text{ nm}$ . These phenomena are usually shown in the series of organometal halide perovskite materials. Additionally, one more feature is supposed to be shown which is an additional emission peak at a lower energy emerges while cooling down. This phenomenon is known to be related to phase transition. However, in our  $\text{CH}(\text{NH}_2)_2\text{Pb}(\text{Br}_{0.6}\text{I}_{0.4})_3$  thin film sample, we cannot find the additional emission peaks, which means there is no phase transition happens while decreasing temperatures. Therefore, based on the above, we were able to confirm that no phase transition occurs, and it is stable as the material itself while the temperature

cooled down.

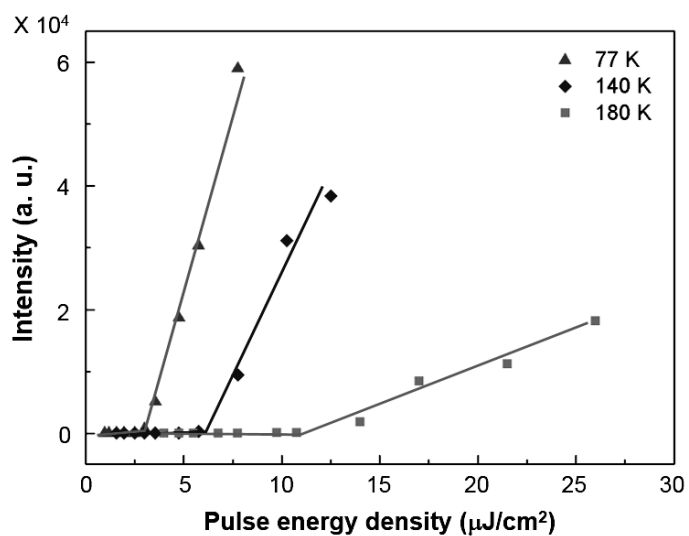


Figure 4-3-3 Temperature-dependent relationship between light input and output of  $\text{CH}(\text{NH}_2)_2\text{Pb}(\text{Br}_{0.6}\text{I}_{0.4})_3$  1D DFB laser for TM mode.

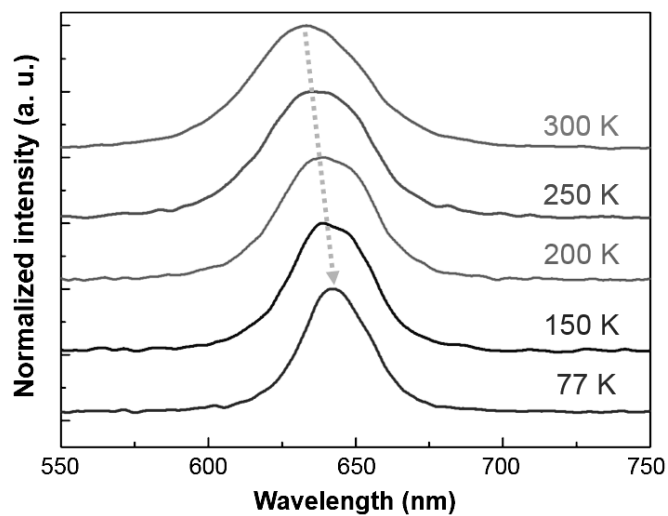


Figure 4-3-4 Temperature-dependent PL spectra of  $\text{CH}(\text{NH}_2)_2\text{Pb}(\text{Br}_{0.6}\text{I}_{0.4})_3$  thin film.

## 4.4 Summary

We demonstrated single mode lasing from organometal lead halide perovskite  $\text{CH}(\text{NH}_2)_2\text{Pb}(\text{Br}_{0.6}\text{I}_{0.4})_3$  with TE/TM mode selection by changing the structural parameters. The single lasing mode comes from DFB structure which is better dynamic-single stability and low noise operation, and this kind of distributed feedback laser is fast to transmit data in optical communication world. Additionally, this mode selection properties are useful in almost every photonic system, especially, in the photonic integrated circuits and their applications. Two kind of devices were designed and fabricated to operate at TE and TM mode under single mode lasing condition. We adopted LIL technique with the submicron scale pattern on large area. In addition, we deposited the hybrid perovskite  $\text{CH}(\text{NH}_2)_2\text{Pb}(\text{Br}_{0.6}\text{I}_{0.4})_3$  thin film on 1D DFB structure by simple spin-casting method with uniform and conformal surface morphology. Both techniques brings us to be competitive advantages in the aspect of fabrication cost and throughput. We believe this hybrid photonics platform can be one possible solution to build up the complicated and sophisticated photonics integrated circuit and their applications.

## 4.5 Supporting information

We also demonstrated single mode lasing at 77 K with different organometal lead halide perovskite thin films such as  $\text{CH}(\text{NH}_2)_2\text{PbBr}_3$ ,  $\text{CH}(\text{NH}_2)_2\text{Pb}(\text{Br}_{0.6}\text{I}_{0.4})_3$ , and  $\text{CH}(\text{NH}_2)_2\text{PbI}_3$ . From  $\text{Br}_3$  and  $\text{I}_3$  based perovskite thin films, we could demonstrate single mode lasing at room temperature. However, with mix halide composition of perovskite thin film, we could not see any lasing characteristics, even a mode at room temperature. We guess this happen because the different lattice mixed in perovskite structure, so that it is unstable in phase transition. Figure 4-5-1 shows the single mode lasing operation with the one-dimensional photonic crystal structure with different grating period at different wavelength regime.

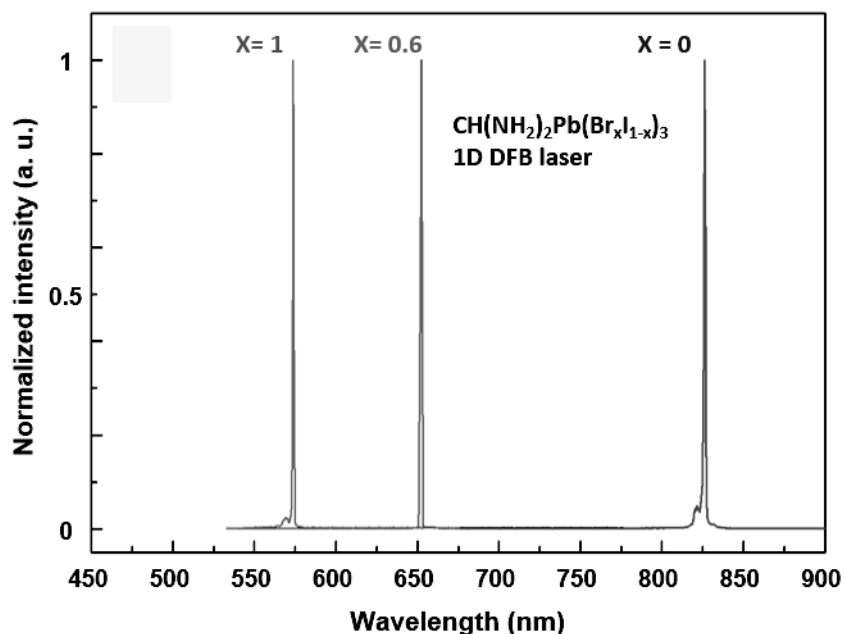


Figure 4-5-1 Single mode lasing operation with the one-dimensional photonic crystal structure at different wavelength regime.

## References

- [1] W. S. Yang, J. H. Noh, N. J. Jeon, Y. C. Kim, S. Ryu, J. Seo, and S. I. Seok, "High-performance photovoltaic perovskite layers fabricated through intramolecular exchange," *Science*, **348**, 1234-1237, (2015).
- [2] S. D. Stranks, G. E. Eperon, G. Grancini, C. Menelaou, M. J. P. Alcocer, T. Leijtens, L. M. Herz, A. Petrozza, and H. J. Snaith, "Electron-hole diffusion lengths exceeding 1 micrometer in an organometal trihalide perovskite absorber," *Science*, **342**, 341-344, (2013).
- [3] G. Xing, N. Mathews, S. Sun, S. S. Lim, Y. M. Lam, M. Grätzel, S. Mhaisalkar, and T. C. Sum, "Long-range balanced electron and hole-transport lengths in organic-inorganic  $\text{CH}_3\text{NH}_3\text{PbI}_3$ ," *Science*, **342**, 344-347 (2013).
- [4] C. Wehrenfennig, G. E. Eperon, M. B. Johnston, H. J. Snaith, and L. M. Herz, "High charge carrier mobilities and lifetimes in organolead trihalide perovskites," *Advanced Materials*, **26**, 1584-1589, (2014).
- [5] F. Deschler, M. Price, S. Pathak, L. E. Klintberg, D.-D. Jarausch, R. Higler, S. Hüttner, T. Leijtens, S. D. Stranks, H. J. Snaith, M. Atatüre, R. T. Phillips, and R. H. Friend, "High photoluminescence efficiency and optically pumped lasing in solution-processed mixed halide perovskite semiconductors," *Journal of Physical Chemistry Letters*, **5**, 1421-1426, (2014).
- [6] G. Xing, N. Mathews, S. S. Lim, N. Yantara, X. Liu, D. Sabba, M. Grätzel, S. Mhaisalkar, and T. C. Sum, "Low-temperature solution-processed wavelength-tunable perovskites for lasing," *Nature Materials*, **13**, 476-480, (2014).
- [7] Z.-K. Tan, R. S. Moghaddam, M. L. Lai, P. Docampo, R. Higler, F. Deschler, M. Price, A. Sadhanala, L. M. Pazos, D. Credgington, F. Hanusch, T. Bein., H. J.

- Snaith and R. H. Friend, "Bright light-emitting diodes based on organometal halide perovskite," *Nature Nanotechnology*, **9**, 687-692, (2014).
- [8] H. Cha, S. Bae, M. Lee, and H. Jeon, "Two-dimensional photonic crystal bandedge laser with hybrid perovskite thin film for optical gain," *Applied Physics Letters*, **108**, 181104, (2016).
- [9] X.-L. Yu, Y. Wang, Y.-M. Hu, C.-B. Cao, and H. L.-W. Chan, "Gas-Sensing properties of perovskite BiFeO<sub>3</sub> nanoparticles," *Journal of the American Ceramic Society*, **92**, 3105-3107, (2009).
- [10] H. Zhu, Y. Fu, F. Meng, X. Wu, Z. Gong, Q. Ding, M. V. Gustafsson, M. T. Trinh, S. Jin, and X.-Y. Zhu, "Lead halide perovskite nanowire lasers with low lasing thresholds and high quality factors," *Nature Materials*, **14**, 636-643, (2015).
- [11] Q. Liao, K. Hu, H. Zhang, X. Wang, J. Yao, and H. Fu, "Perovskite microdisk microlasers self-assembled from solution," *Advanced Materials*, **27**, 3405-3410, (2015).
- [12] S. Chen, W. K. Chong, J. Lee, K. Roh, E. Sari, N. Mathews, T. C. Sum, and A. Nurmikko, "Optically Pumped Distributed Feedback Laser from Organo-Lead Iodide Perovskite Thin Films," in *CLEO: 2015, OSA Technical Digest (online)* (Optical Society of America, 2015), paper SM2F.6.
- [13] R. Dhankar, A. N. Brigeman, A. V. Larsen, R. J. Stewart, J. B. Asbury, and N. C. Giebink, "Random lasing in organo-lead halide perovskite microcrystal networks," *Applied Physics Letters*, **105**, 151112, (2014).
- [14] C. C. Stoumpos, C. D. Malliakas, and M. G. Kanatzidis, "Semiconducting tin and lead iodide perovskites with organic cations: phase transitions, high mobilities, and near-infrared photoluminescent properties," *Inorganic Chemistry*,

- 52**, 9019-9038, (2013).
- [15] Y. Han, S. Meyer, Y. Dkhissi, K. Weber, J. M Pringle, U. Bach, L. Spiccia, and Y.-B. Cheng, "Degradation observations of encapsulated planar  $\text{CH}_3\text{NH}_3\text{PbI}_3$  perovskite solar cells at high temperatures and humidity," *Journal of Materials Chemistry A*, **3**, 8139-8147, (2015).
- [16] R. K Misra, S. Aharon, B. Li, D. Mogilyansky, I. Visoly-Fisher, L. Etgar, and E. A Katz, "Temperature-and component-dependent degradation of perovskite photovoltaic materials under concentrated sunlight," *The journal of Physical Chemistry Letters*, **6**, 326-330, (2015).
- [17] B. Conings, J. Drijkoningen, N. Gauquelin, A. Babayigit, J. D'Haen, L. D'Olieslaeger, A. Ethirajan, J. Verbeeck, J. Manca, and E. Mosconi, "Intrinsic thermal instability of methylammonium lead trihalide perovskite," *Advanced Energy Materials*, **5**, 1500477, (2015).
- [18] T. M. Koh, K. Fu, Y. Fang, S. Chen, T. C. Sum, N. Mathews, S. G Mhaisalkar, P. P Boix, and T. Baikie, "Formamidinium-containing metal-halide: An alternative material for near-IR absorption perovskite solar cell,." *The Journal of Physical Chemistry C*, **118**, 16458-16462, (2013).
- [19] S. Pang, H. Hu, J. Zhang, S. Lv, Y. Yu, F. Wei, T. Qin, H. Xu, Z. Liu, and G. Cui, " $\text{NH}_2\text{CH}=\text{NH}_2\text{PbI}_3$ : An alternative organolead iodide perovskite sensitizer for mesoscopic solar cells," *Chemistry of Materials*, **26**, 1485-1491, (2014).
- [20] G. E Eperon, S. D Stranks, C. Menelaou, M. B Johnston, L. M Herz, and H. J Snaith, "Formamidinium lead trihalide: a broadly tunable perovskite for efficient planar heterojunction solar cells," *Energy & Environmental Science*, **7**, 982-988, (2014).

- [21] J.-W. Lee, D.-J. Seol, A.-N. Cho, and "High-efficiency perovskite solar cells based on the black polymorph of  $\text{HC}(\text{NH}_2)_2\text{PbI}$ ," *Advanced Materials*, **26**, 4991-4998, (2014).
- [22] J. H. Noh, S. H. Im, J. H. Heo, T. N Mandal, and S. I. Seok, "Chemical management for colorful, efficient, and stable inorganic–organic hybrid nanostructured solar cells," *Nano Letters*, **13**, 1764-1769, (2013).
- [23] J.-H. Seo, J. H. Park, S.-I. Kim, B. J. Park, Z. Ma, J. Choi, and B.-K. Ju, "Nanopatterning by laser interference lithography: applications to optical devices," *Journal of Nanoscience and Nanotechnology*, **14**, 1521-1532, (2014).
- [24] N. J. Jeon, J. H. Noh, Y. C. Kim, W. S. Yang, S. Ryu, and S. I. Seok, "Solvent engineering for high-performance inorganic–organic hybrid perovskite solar cells," *Nature Materials* **13**, 897-903, (2014).
- [25] N. Ahn, D.-Y. Son, I.-H. Jang, S. M. Kang, M. Choi, and N.-G. Park, "Highly reproducible perovskite solar cells with average efficiency of 18.3% and best efficiency of 19.7% fabricated via Lewis base adduct of lead (II) iodide," *Journal of the American Chemical Society*, **137**, 8696-8699, (2015).
- [26] H. Kim, H. Jung, D.-H. Lee, K. B. Lee, and H. Jeon, "Period-chirped gratings fabricated by laser interference lithography with a concave Lloyd's mirror," *Applied Optics*, **55**, 354-359, (2016).



# Chapter 5

## Conclusion and Perspective

In this thesis, I have been focused on demonstrating the different types of photonics crystal bandedge lasers with different gain materials including the hybrid perovskite materials. Firstly, air-bridge-type surface-emitting bandedge laser (BEL) was fabricated by forming a honeycomb lattice two-dimensional photonic crystal (PhC) structure into an InGaAsP multiple quantum well (MQW). Subsequently, the entire surface of bandedge laser was passivated with few-nm thick conformal SiO<sub>2</sub> layer by atomic layer deposition (ALD) method. In addition, the ALD-SiO<sub>2</sub> is compatible with the silane-based surface chemistry, enabling the ALD-passivated BEL devices as a label-free biosensor. The standard streptavidin–biotin interaction was examined to see the possibility of the device as biosensor. Consequently, the device shows the possibility as refractive index biosensor platform with a sharp lasing line (< 0.2 nm) and large refractive index sensitivity (~163 nm/RIU).

Next, I suggested *hybrid photonic* platforms, in which passive photonic structures are hybridized extrinsically with active optical materials, for demonstrating a single mode laser with hybrid perovskite thin film. At first, the room temperature single mode lasing from the hybrid perovskite CH<sub>3</sub>NH<sub>3</sub>PbI<sub>3</sub>, which is at the center emission wavelength of  $\lambda = 780$  nm, was successfully demonstrated. In this study, a single lasing mode was originally defined by a bandedge mode of 2D square lattice PhC backbone structure, while optical gain necessary for laser action was provided by a thin hybrid perovskite film spin-coated on top of the PhC backbone. Also, two different bandedge lasers operating at  $\Gamma$ - and M-points were designed and fabricated to operate as single mode bandedge lasers. Therefore, both devices lased in single

mode with the polarization properties expected from the bandedge modes. On the other hand, from the hybridizing the hybrid perovskite  $\text{CH}(\text{NH}_2)_2\text{Pb}(\text{Br}_{0.6}\text{I}_{0.4})_3$  thin film, which is at the center emission wavelength of  $\lambda = 650$  nm, with one-dimensional photonic crystal structure backbone by simple spin-casting, single mode bandedge lasers were also demonstrated. In this study, two kinds of devices were designed and fabricated to operate at TE and TM mode under single mode lasing condition. From the experiment, we confirmed the devices operating under single mode lasing condition and revealed TE/TM polarization dependence, respectively.

The benefits of photonics crystal bandedge lasers are as follows; stable mode operation over a large area, high power laser available, and controlling the lasing direction either surface-emitting or in-plane direction which depends on its purpose of devices. With these advantages, I believe that our surface-passivated  $\Gamma$ - point BEL can be a great option for the compact and ultrasensitive biosensor platforms based on nanophotonics technology due to the high figure-of-merit (FOM) value and sharp resonance peak. Also, the results of these hybrid photonic device platforms with optical pumping show the possibility of electrically driven laser device with hybrid perovskite materials in the near future.

## 국문 초록

광자결정은 굴절률이 서로 다른 두 가지 이상의 물질을 주기적으로 배열한 광학 구조를 이야기 한다. 광자결정의 주기성에 의해서 생성된 광 밴드구조 내에서는 어떠한 모드도 존재할 수 없는 주파수 영역이 존재를 하는데 이 영역을 광 밴드갭이라고 이야기 한다. 이는 마치 전자가 고체 결정을 이루는 원자들의 주기적인 포텐셜에 의해 영향을 받아서 특정 에너지를 가질 수 없는 밴드를 형성하는 것과 유사한 메커니즘으로 이해를 할 수 있다. 이러한 광 밴드갭을 이용하게 되면 빛을 강하게 가둘 수가 있고 이를 이용하면 다음과 같은 캐비티, 필터, 도파로 등의 응용이 가능하다. 반면 밴드구조 내에 있는 밴드에지 근처에서는 광자의 군속도가 거의 영에 가까워지게 되며 이것을 통해 정상파가 형성이 된다. 이 경우 물질과 빛의 상호작용이 크게 증가하게 되며 이러한 효과를 응용하여 포토닉 밴드에지 레이저를 구현할 수 있게 된다. 포토닉 밴드에지의 경우 안정적인 모드의 형성과 이를 통한 높은 출력의 레이저 구현이 가능하다. 또한, 레이저의 방향성을 구조의 디자인에 따라 조절 할 수 있다는 장점을 가지고 있다.

본 학위 논문에서는, 먼저 1.5  $\mu\text{m}$  영역대의 InGaAsP 다중양자우물에 광자결정 구조를 이용하여 수직발광 형의 밴드에지레이저를 구현하였다. 또한, 여기에 원자층 증착 방법을 통한 얇은 실리콘 옥사이드를 증착함을 통해서 바이오센서 플랫폼으로서의 활용을 준비할 수 있었다. 간단한 스트렙타아비딘과 바이오틴의 바이오실험을 통해서 실제 샘플이 바이오센서로서의 활용이 가능한지를 확인 하였으며 얇은 반측폭을 통한 높은 성능지수 (figure of merit)를 통해서 다른 바이오 센서를 대체할 수 있는 좋은 대안이 될 것으로 기대를 하고 있다.

그리고 물질적으로는 최근 태양전지 분야에서 활발히 연구가 되고 있는 페로브스카이트 물질을 선택하여 2차원 광자결정구조와 1차원 DFB 구조의 결합을 통한 밴드에지 레이저를 순차적으로 구현하였다. 이번 연구에서는 간단한 스핀코팅 방법을 통해서 methylammonium lead triiodide 페로브스카이트 물질을 성장시켰으며 그것을 통하여 먼저 상온에서 구동하는 단일 파장 (780 nm 파장)의 2차원 광자결정 밴드에지 레이저를 만들 수 있었다. 또한, 2차원 광자결정 밴드에지 구조와 물질의 결합을 통해서 서로 다른 파수 백터를 지니는 밴드에지 레이저를 디자인 하였으며 실제 계산 결과와 실험 결과를 통해서 그것을 확인할 수 있었다.

이후, 가시광 영역에서 빛을 내는 페로브스카이트 물질과 1차원 DFB 구조의 결합을 통해서 650 nm 파장에서 구동하는 단일 파장 레이저를 저온 실험을 통해서 확인할 수 있었다. 간단한 구조의 변화, 즉 주기의 변화만으로도 서로 다른 편광 방향을 지닌 레이저를 구현할 수 있었으며 앞서 연구와 마찬가지로 간단한 스핀 코팅 방법을 통해서 구조 위에 물질을 성장하였다. 하지만, 이번의 경우 앞선 연구와는 다르게 페로브스카이트 물질에 쓰이는 용매들 즉, DMSO와 DMF의 비율 조건을 최적화 함으로써 더 균일하고 좋은 박막을 형성할 수 있었다. 이번 연구의 경우 formamidinium을 기반으로 한 페로브스카이트 물질을 간단한 스핀코팅을 통해 구현한 가시광 영역에서의 첫 번째 단일 파장 레이저라는데 의의가 있다. 페로브스카이트 물질 응용을 통하여 구현된 레이저들의 경우 패시브 광자결정 구조와 액티브 물질간의 결합을 통하여 구현한 하이브리드 레이저 구조로서 연구를 통해 나타난 결과가 앞으로의 복잡한 광집적 회로에 좋은 대안 중 하나가 될 수 있을 것으로 기대를 하고 있다.

**핵심어:** 광자결정, 밴드에지, 광자결정 레이저, 원자층 증착, 바이오센서, 페로브스카이트, 2차원 광자결정, 1차원 광자결정, 하이브리드 레이저

**학번:** 2010-24018